CHALMERS
UNIVERSITY OF TECHNOLOGY

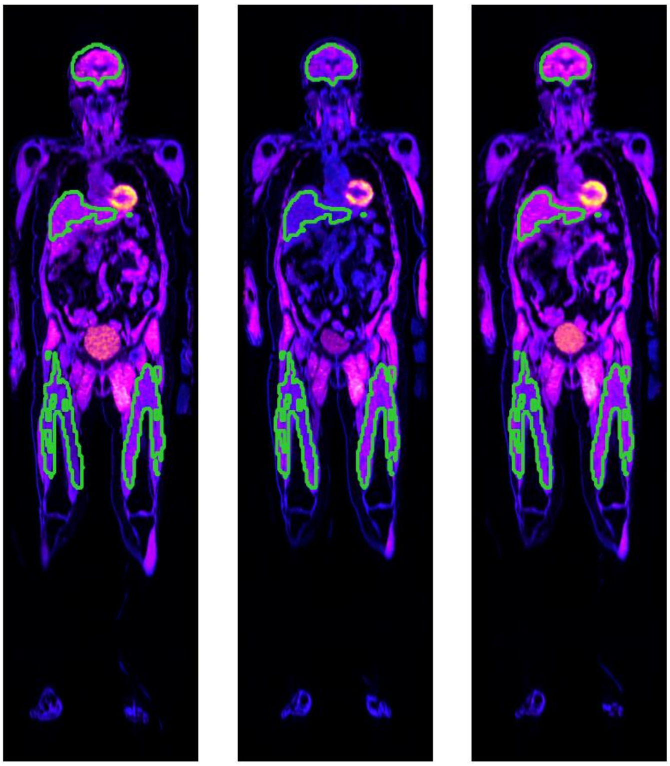

Motion Correction for Dynamic PET/MR Datasets

Image Registration for Post-Reconstruction Whole-Body MR Images

Master’s thesis in Electrical Engineering

EMELIE SVENSSON
ANNA VON SYDOW

DEPARTMENT OF ELECTRICAL ENGINEERING

CHALMERS UNIVERSITY OF TECHNOLOGY
Gothenburg, Sweden 2023

Master's thesis 2023

Motion Correction for Dynamic PET/MR Datasets

Image Registration for Post-Reconstruction Whole-Body MR Images

Emelie SVENSSON
Anna VON SYDOW

Department of Electrical Engineering
Chalmers University of Technology
Gothenburg, Sweden 2023

Motion Correction for Dynamic PET/MR Datasets
Image Registration for Post-Reconstruction Whole-Body MR Images
Emelie SVENSSON
Anna VON SYDOW

© EMELIE SVENSSON, 2023.
© ANNA VON SYDOW, 2023.

Supervisor: Simon Ekström, Antaros Medical
Supervisor: Iina Laitinen, Antaros Medical
Examiner: Ida Häggström, Electrical Engineering

Master's Thesis 2023
Department of Electrical Engineering
Chalmers University of Technology
SE-412 96 Gothenburg
Telephone +46 31 772 1000

Cover: Fused PET/MR images with segmentations for brain, liver, left and right quadriceps femoris muscle.

Typeset in LaTeX
Gothenburg, Sweden 2023

Motion Correction for Dynamic PET/MR Datasets
Image Registration for Post-Reconstruction Whole-Body MR Images
EMELIE SVENSSON
ANNA VON SYDOW
Department of Electrical Engineering
Chalmers University of Technology

Abstract

Positron emission tomography (PET) is an imaging technique that uses short lived radioactive labelled molecules to visualise and measure physiological activities. Dynamic PET acquisition requires a long scan time, and movement of the subject during this time cannot be fully avoided. Motion of organs due to breathing, heartbeat, etc. is continuous, but there are also bulk motions of body regions to consider which may occur if the subject has difficulty laying still. Motion of subjects during a PET scan is an important factor that degrades image resolution and quality, and thereby limits its potential to provide accurate readouts. Therefore, this study aimed to implement an approach for motion correction of a dynamic whole-body hybrid PET/MR dataset.

The method consisted of utilising a deformable image registration in a post-reconstruction approach on the MR images to find optimal displacement fields, and then applying these on the PET images. The registration method used in this study was fast graph-cut based optimisation, which was evaluated with Dice score and properties of the displacement field. The transformed PET images were evaluated with Patlak modelling and visualised with segmentations.

Results regarding the image registration part show an improvement in terms of Dice score and reasonable properties of the displacement fields. For the motion corrected PET images there is a visual difference for images containing considerable motion. There is also a decrease in error of the Patlak slope fit in the Patlak modelling, indicating an improvement of the correct localisation of the segments over time. The conclusion is that the used method gives promising results for the studied dataset, however further research is needed with larger datasets that also contain a wider range of movements.

Keywords: "PET/MR", "Motion Correction", "Image registration", "Whole-Body", "Dynamic PET".

Acknowledgements

First, we would like to thank Antaros Medical for giving us this opportunity and for providing an interesting project. Special thanks to our supervisors Simon Ekström and Iina Laitinen for their time and support throughout this project. Also thanks to Carl Sjöberg for a warm welcome and guidance. We would also like to thank Ida Häggström for being our examiner and cheering us on.

Emelie Svensson & Anna von Sydow, Gothenburg, 2023-06-08

Contents

Nomenclature

Abbreviations

CC	Cross Correlation
CT	Computed Tomography
DICOM	Digital Imaging and Communications in Medicine
DSC	Dice Similarity Coefficient
FDG	[^{18}F]Fluorodeoxyglucose
GCP	Good Clinical Practice
GPU	Graphics Processing Unit
HEC	Hyperinsulinemic Euglycemic Clamp
ICM	Iterated Conditional Modes
MI	Mutual Information
MR	Magnetic Resonance
MRAC	Magnetic Resonance based Attenuation Correction
NCC	Normalised Cross Correlation
NRRD	Nearly Raw Raster Data
PET	Positron Emission Tomography
RF	Radiofrequency
RSE	Relative Standard Error
SSD	Sum of Squared Distances

Segmentation Names (PET)

lquad	left quadriceps femoris muscle
myoc	myocardium
panc	pancreas
rquad	right quadriceps femoris muscle

sat	subcutaneous adipose tissue
vat	visceral adipose tissue

List of Figures

List of Tables

1

Introduction

Positron emission tomography (PET) is an imaging technique that uses short lived radioactive labelled molecules, so called radiotracers, to visualise and measure physiological activities. Dynamic PET provides a time series of 3D images that contain information of the activity distribution of the radiotracer. For accurate dynamic measurements, the PET data is acquired over a period of time suitable for the radiotracer in question, and quantified using modelling. During the long scan time for dynamic PET, movement of the subject cannot be fully avoided. Motion due to respiratory motion, cardiac contraction or motion of internal organs are naturally occurring, but there is also bulk motions of body regions (e.g. head, arms, legs and torso). These bulk motions may occur if the subject has difficulty laying still during the long scan time.

Motion of subjects in PET is an important factor that degrades image resolution and quality, and thereby limiting its potential of accurate readouts. Motion can cause false readouts, a voxel that previously represented a specific point in the anatomy, might not represent the same location throughout the time series. Movements could then cause a decrease in the accuracy of the results, by complicating the analysis of tissues when they are not in the same location over time. PET is usually combined with computed tomography (CT), but there are also hybrid PET/MR (magnetic resonance) cameras. The information is used for attenuation correction, anatomical reference and also to estimate motion. By applying a motion correction algorithm to a dynamic dataset, the effect of motion could potentially decrease and lead to improved image quality. [1]

Image registration is an image processing technique where two or more images are aligned into spatial correspondence. Fast graph-cut based optimisation for practical dense deformable registration of volume images, has been introduced as a method which can achieve a significant reduction in computational time [2]. This makes graph-cut based deformable registration of large volume images feasible. The presented method is shown to work well for large medical volume images, specifically whole-body MR images. In regards of whole-body imaging, it provides possibilities to assess physiological functions and diseases spread in the whole-body, e.g. to evaluate metastatic disease or the effect of treatment in drug development [3][4].

There are other motion correction methods that has been implemented in PET/MR datasets, such as rigid motion correction [5]. It has been implemented for head motion and shows promising results. However, the assumption of a rigid body may not work as well for other parts of the body, such as soft tissue. Moreover, other studies have implemented motion correction before or during reconstruction [6][7]. Although, for already reconstructed datasets without access to the the raw data, only methods that apply motion correction post-reconstruction is applicable.

This study aims to investigate potential approaches for motion correction and evaluate them. Implementation will be done on dynamic whole-body PET/MR datasets that has been previously acquired. The study is based on a published method of acquiring dynamic whole-body PET/MR datasets to evaluate insulin mediated glucose flux in tissues, using ^{18}F-FDG (fludeoxyglucose) as radiotracer and the Patlak model [8]. The Patlak model is an example of a graphical analysis technique for PET modelling, to extract the net influx rate of irreversible uptake of a radiotracer [9][3]. In the dataset used for the implementation, a simultaneous MR imaging is performed at the same time as PET, for five repeated times over the course of the FDG accumulation. This allows to utilise these MR images to compensate for the motion during this total scan time, and apply the same coordinate and transformations to PET. During the circa one hour long protocol for these datasets, there were body movements occurring. These movements are difficult to compensate for manually and may affect the image quantification by kinetic modelling.

1.1 Aims

The project aims to implement an approach for motion correction of a dynamic whole-body PET/MR dataset, using image registration of sequentially acquired MR images. To achieve this aim, a method to evaluate the accuracy will also be investigated and implemented. The second objective is to evaluate image registration and how motion correction affects the result of the quantitative endpoint in the PET quantification. More specifically, how the Patlak parameters influx flow and goodness of fit are affected in tissues with observed motion. Furthermore, the result may also provide clarity on how motion correction impacts the results of dynamic PET modelling.

1.2 Scope

The scope of this study is limited to methods that can be applied to datasets acquired with hybrid PET/MR imaging and a dynamic protocol. More specifically it is limited to the methods of applying motion correction to the MR datasets and then using it on the corresponding PET images. It is also limited to post-reconstruction motion correction. Furthermore, the implementation of this study will focus on correcting for bulk motion of body regions. However, motion due to respiratory, cardiac contraction or motion of internal organs, are covered briefly in the theory and discussion.

There have been previous studies on motion correction for PET/MR, mostly regarding periodic motions such as respiratory and cardiac, but also for brain with rigid transformation [1]. What separates this work from others is the unique dataset it will be applied on and the type of motion this study aims to correct. Dynamic whole-body PET/MR is a relatively new method and no commercial solution is readily available for motion correction of bulk motions for these types of datasets.

2

Theory

This chapter is dedicated to give an understanding of relevant parts of medical imaging, types of motion occurring during data acquisitions and image registration.

2.1 Medical Imaging

The term "medical imaging" covers the techniques that allow us to view the interior of the body [10]. It can be used for clinical analysis as well as for research purposes. This section will present the imaging modalities relevant to this study, more specifically PET, MR and hybrid PET/MR. Furthermore, it will present the Patlak model used for graphical analysis of dynamic PET.

2.1.1 MR

Magnetic resonance (MR) imaging is an imaging method based on nuclear magnetic resonance. In strong magnetic fields, protons aligns with the field. Since the body consists of a large number of hydrogen atoms, and therefore protons, the body becomes magnetised in strong magnetic fields. With a radiofrequency (RF) pulse, it is possible to excite many of the protons to align against the magnetic field. After the pulse, the protons realigns with the magnetic field of the MR through relaxation processes, and also emits RF energy. The emitted signals are measured by an antenna in the MR device. The frequency information in the signals is reconstructed to intensity levels with Fourier transforms, and are displayed as shades of gray in the image. Different types of images can be created by varying the sequence of RF pulses applied and measured. [11]

Tissues can be characterised by different relaxation times. The longitudinal relaxation time (T1) is the recovery of the longitudinal magnetisation back to its initial value, and is caused by the spins transferring energy to the surrounding. Transverse relaxation time (T2) is caused by perturbations in the magnetic field due to other nearby spins, leading to rephrasing of the transverse magnetisation. The proton density in the tissue therefore affect these relaxation times. [11]

The most common MR sequences are T1-weighted and T2-weighted scans. They are produced using different repetition and echo times between the RF pulse. For example, fat appears bright (high signal intensity) on T1 weighted images and dark on T2-weighted images. It is the opposite for water and fluids. Therefore, T1-weighted images are used to visualise normal soft-tissue anatomy and fat, whereas T2-weighted images are better at visualising fluid and abnormalities. In practice, both types are used to complement each other. Besides the T1 and T2 scans, there are other MR protocols, for example Dixon techniques used to separate fat and water [12]. However, there exists challenges when separating fat and water, for example so called fat-water swaps may occur [13].

Unlike many other imaging modalities, no radiation is produced during an MR exam. Compared to computed tomography (CT), MR produces images of better soft tissue contrast.

2.1.2 PET

Positron emission tomography (PET) is an imaging modality that involves injection of radioactive substances (radiotracers) into the body. When a PET-radiotracer decays it emits positrons, positively charged particles. These positrons travel a short distance in the body and then collide with negatively charged electrons, annihilation produces two gamma rays that are emitted in opposite directions. The PET scanner detects these gamma rays and uses computer algorithms to create detailed images of the radiotracer distribution in the body. A PET scan involves, unlike MR imaging, exposure to radiation. [11]

PET is used to diagnose and stage a wide range of diseases, including cancer, heart disease, and neurological disorders, as well as to monitor the effectiveness of treatment. Furthermore, it can provide insights into the function and metabolism of tissues and cells. Radiotracers are designed to target specific tissues or targets in the body, or to follow blood flow.

PET imaging is typically performed to generate static images containing only one time point. The method involves intravenous injection of PET tracers, and imaging is performed after tracer has distributed to targets and cleared out from blood, in a so called static scan. The generated data can be analysed visually, or used to calculate for example standardised uptake value. [14]

In dynamic protocols PET data is acquired over a period of time, starting from the injection of the PET tracer, instead of a single time point. The time interval depends on which radiotracer is used and which metabolic or physiological process is studied. Dynamic PET acquisition is generally confined to a single bed-position, where the scanner's axial extent limits the field of view to typically 15-25 cm. However, there are methods for dynamic whole-body PET imaging. The combination of dynamic PET and whole-body imaging provides possibilities to assess physiological functions and diseases spread in the whole-body. [3]

Dynamic whole-body PET data is acquired with multi-bed, non-continuous (sparse) scanning over time. The sparse data acquisition can result in the generation of noisy images, but with current PET scanners it is now possible to acquire high quality images with frame durations down to 30 s/bed. Therefore, it is possible to generate dynamic whole-body PET data in reasonable scan times. An illustration of an example of whole-body PET acquisition is shown in figure 2.1. In the figure, seven different bed positions, moved in a cranio-caudal direction, are used to create one whole-body image. The process can then be repeated to create a whole-body set. The same acquisition method can be used for sequential MR imaging. [3]

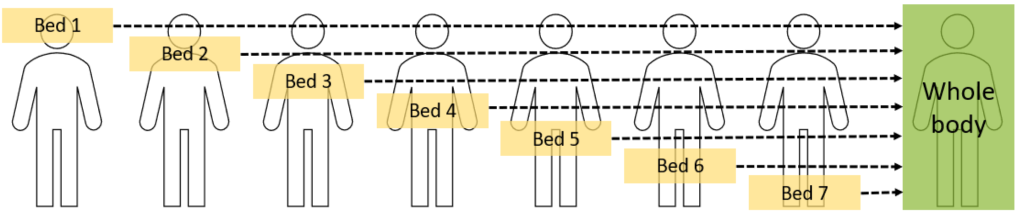

Figure 2.1: Acquisition of one whole-body image.

Before the whole-body scan, as shown in figure 2.1 and also the whole acquisition process in figure 2.3, an initial single-bed dynamic scan over the cardiac region is performed for around 10 minutes [8]. The dynamic cardiac scan is used to extract the early tracer dynamics in the blood plasma [3]. Blood samples are taken between the following whole body scans to measure the activity in the plasma. The data acquired from this protocol can be modelled with Patlak, further explained in section 2.1.3.

Radiotracer FDG

^{18}F fludeoxyglucose (FDG) is a commonly used radiotracer. It is a glucose molecule where one of the hydroxyl groups has been substituted by a Fluorine-18 atom [15]. Similarly to glucose, FDG is also taken up by the cells when they consume glucose. It undergoes an initial metabolic transformation (phosphorylation), that prevents it from leaving the cell again. The second step of glycolysis (or, utilisation of glucose for energy) is prevented in FDG by the fluorine in the position. Therefore, the FDG-molecule (FDG-6-F) remains trapped in the cell, together with other FDG-molecules. This accumulates the radiolabelled substance and the radioactive signal increases. The uptake of FDG in the tissues can be illustrated in a two-tissue compartmental model, shown in figure 2.2 [3]. The FDG partly gets eliminated via the urinary tract. Normally the (static) PET scan is made around 60 minutes after injection to allow the tracer to be absorbed by the tissues, and thereby receive better tissue to blood contrast. [16].

Figure 2.2: Two-tissue compartment model for FDG.

FDG is injected intravenously, normally with a dose of about 350 MBq [15]. All cells that consume glucose will trap the FDG-molecules. Some of the organs that can be seen when using FDG are the brain, the heart and the muscles. In addition, tumours and their metastases can also be distinguished because of their rapid growth and proliferation. From the dynamic course of the ^{18}F-FDG, spatial distribution in the tissues may reveal useful clinical information on tissue's metabolic properties [17]. For example, the metabolic rate of glucose uptake can provide information of physiology or patient groups.

2.1.3 Patlak Model

Glucose uptake in tissues can be estimated by calculating kinetic rate of FDG in the tissues using the model introduced by Patlak. [9][3]. The Patlak model is applicable for irreversible binding of a two compartment model, which is shown in figure 2.2. As the figure shows, there has to be at least one irreversible step where the radiotracer is trapped [18]. An illustration of how the Patlak model is applied on the raw data acquired from the scanning protocol is shown in figure 2.3. Before steady-state is reached there are initially sharp concentration changes, shown in the time activity curve in figure 2.3. When the steady-state is reached, the Patlak plot becomes linear and the Patlak slope and intercept are estimated for every region or voxel of interest, shown in the bottom of figure 2.3.

The radiotracer concentration at time t in a tissue region or voxel of interest can be denoted as $C_T(t)$ and radiotracer concentration in the plasma (input function) as $Cp(t)$. These are the curves in the middle graph in figure 2.3. The Patlak plot is calculated from the linearity between the normalised tissue concentration and normalised integral of $Cp(t)$ after the time of steady-state t^* is reached. The linear formulation is

$$\frac{C_T(t)}{C_p(t)} = K_i \frac{\int_0^t C_p(\tau)d\tau}{C_p(t)} + V \quad (t > t^*) \tag{2.1}$$

where K_i, the slope, is the radiotracer influx or uptake rate constant [18]. V, the Patlak intercept, can be referred to as the total blood plasma distribution volume. The data can then be plotted from

$$y(t) = \frac{C_T(t)}{C_p(t)} \tag{2.2}$$

and

$$x(t) = \frac{\int_0^t C_p(\tau)d\tau}{C_p(t)} \tag{2.3}$$

for each time point, and fit the data using equation 2.1. Linear regression is then used to estimate the slope K_i and the intercept V [19]. To determine the accuracy of the model, the standard error of K_i, $K_{i_{se}}$, and the relative standard error (RSE) can be used. The $K_{i_{se}}$ can be formulated as

$$K_{i_{se}} = \frac{\sigma}{\sqrt{n}} \tag{2.4}$$

where σ is the standard deviation and n is the sample size (i.e. the number of time points). Further, the RSE then can be described as

$$RSE = \frac{K_{i_{se}}}{K_i} \cdot 100 \tag{2.5}$$

where 100 is multiplied for the results to be in percent. Since the RSE is divided by K_i it is easier to use when comparing different sets.

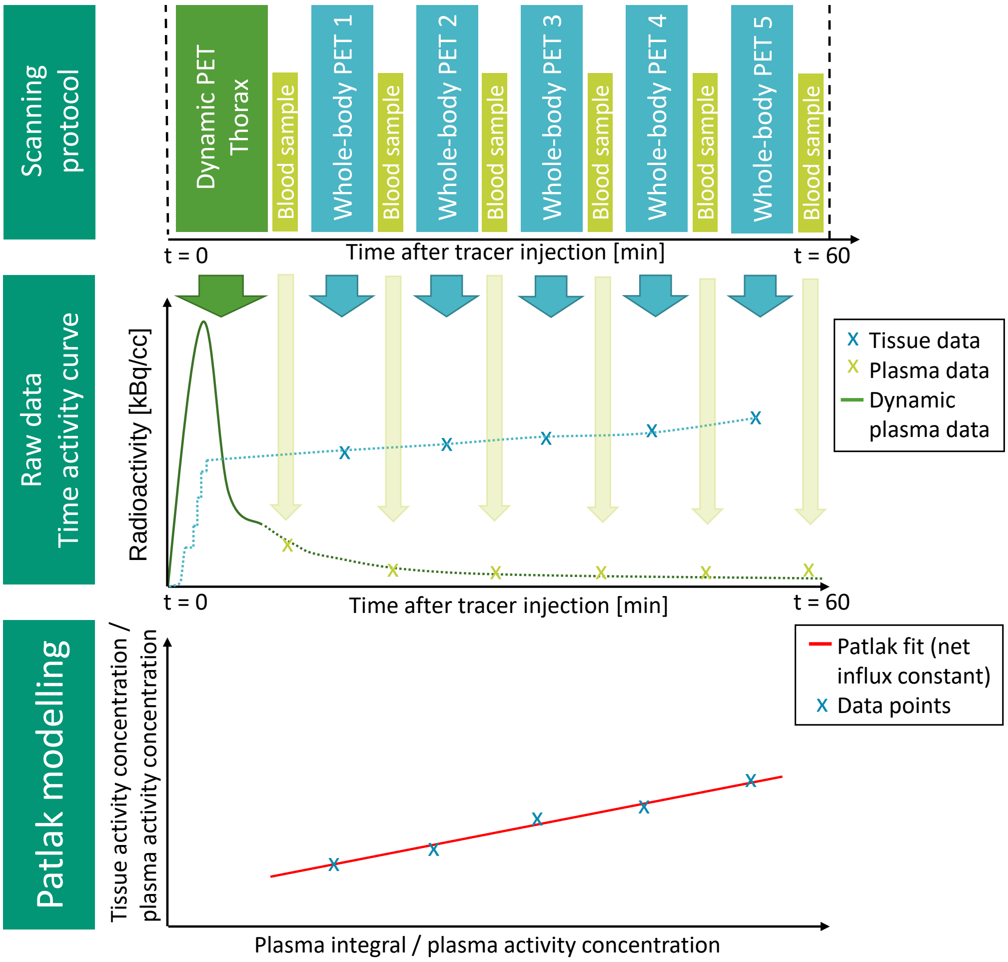

Figure 2.3: An illustration of Patlak modelling and how it is calculated from the whole-body scanning protocol. The illustration is to show the general concept of modelling with Patlak.

2.1.4 PET/MR

Hybrid PET/MR is a growing imaging modality for both clinical and research applications [20][21][22]. Simultaneous acquiring of PET/MR combines the strengths of each modality, enabling imaging of physiology with the high molecular sensitivity of PET, complemented with the high resolution anatomical information of MR imaging. Another advantage of hybrid imaging is the possibility to receive the anatomical reference for attenuation correction for PET, due to most of the emitted photons being attenuated (absorbed) in the body.

The first clinical whole-body PET/MR systems were installed in 2010, although the current standard PET modality is PET/CT, but the number of PET/MR is also growing [23]. Compared to CT, MR imaging provides superior soft-tissue contrast, as well as lower radiation exposure, which is an advantage especially for pediatric applications and protocols that require serial imaging (e.g. dynamic whole-body). Simultaneous PET/MR offers opportunities to quantify physiological processes that otherwise would be difficult to assay with either modality alone.

2.2 Types of Motion

When scanning a living subject for a long period of time, motion of the subject is inevitable. This is a considerable problem in PET studies, where long acquisition times are required for acquiring a large number of coincidence events, and thereby reconstructing good quality images [24]. Motions such as physiological (motion of vital organs) or spontaneous (movements of body regions), both affects the quality of the acquired data [1]. The displacement due to motion, compared to the resolution of the current PET imaging, can substantially affect the diagnostic and quantitative accuracy. Motion is inevitable and gets more noticeable when the scan time is extensive [1]. The following sections clarifies for the different types of motion that may occur during a scan.

2.2.1 Bulk Motions

Bulk motions of body regions include movement of head, arms, legs, shoulders and torso. Movement of these regions may occur due to discomfort. This may also give a shift of the internal organs. A common occurring motion is movement of the head, which can give a considerable displacement. For patients with neurodegenerative diseases or non-anaesthetised children, the displacement may be even larger. There is also movement of the jaw and tongue, which can be complex to correct for. Movements of the limbs are to some extent restricted during PET/MR, because of the coils surrounding the body. However, even with the coils, subjects with claustrophobia tend to move during substantial acquisition time. [1]

2.2.2 Cardiac Contraction

Cardiovascular contraction can considerably affect the quality of acquired data regarding the heart and the vascular system. That is motion from the ventricles, making blood pump throughout the circulatory system. Even though these motions are quite periodic, it is still challenging to correct because of the complexity of the contraction itself. To minimise the effect of cardiac motions can its periodicity be utilised. This is known as cardiac gating, which is a technique that controls the image acquisition by electrical signals, monitoring the cardiac cycle. This enables to acquire images from the same part in the cardiac cycle. However, modelling cardiac motion gets even more complex together with respiratory motion. [1]

2.2.3 Respiratory Motion

Respiration is a common source of motion, which displaces and deforms surrounding organs. Correcting for respiratory motion is difficult since it is not periodic and how the surrounding organs displace and deform differ. It can also affect organs that are far away by causing a repetitive motion due to the respiration. The displacement of the diaphragm during shallow breathing estimates to $15 - 20$ mm, which may give blurring and distortions in the images [1]. For short acquisition in MR imaging, subjects are then often asked to hold their breath to minimise distortions.

2.2.4 Motion of Other Internal Organs

A living subject has a constant flow of fluids within the body. Swallowing, peristalsis, filling of the bladder during the data acquisition and displacement of gas pockets in the intestinal tract, all generate movements [24]. These motions are not that substantial in respect to the PET resolution for short static scans, but more profound for more extensive acquisitions and may then affect the imaging of these organs and their surroundings [1].

2.3 Image Registration

Image registration is of importance in numerous aspects of medical image analysis [25]. The process of image registration is to bring two or more images into spatial correspondence [26]. With the focus of pairwise registration, one of the images is often chosen as reference and the other as moving image. The moving image is then registered against the reference image. The goal of the registration is to find the optimal transformation that aligns the two images [26]. Finding the optimal transformation is done with respect to some similarity metric. The following sections describes the three main components of image registration, which are transformation models, similarity metrics and optimisation strategy. Then there is also a section regarding motion correction.

2.3.1 Transformation Models

Regarding the success of a registration algorithm, the choice of transformation model is of high importance and highly dependent on the characteristics of the data used [27]. Interpolation in image registration is where a point is mapped from one image space to another by a transformation [27]. The new position is generally not bound by the image grid, and therefore an evaluation of the image intensity at the new position is needed. The interpolation solution can affect the accuracy and speed of the registration process, and thus a simpler interpolation algorithm is often used in the optimisation step [27]. Nearest neighbour and linear interpolation are two examples of such algorithms. This section describes some transformation models relevant for this study, which are rigid, affine and deformable transformation.

Rigid Transformation

The rigid transformation model is one of the simplest forms of transformation, regarding image registration [25]. The model consists of aligning two images by finding the rotations and translations that optimise some similarity metric of the images. Translation moves the set of points for some fixed distance and rotation is done by rotating the set of points with respect to the origin [28]. Figure 2.4 shows the concept of a rigid transformation, with some rotation θ. In medical image registration, rigid transformation models are mainly used in either registration of rigid structures (e.g. bones) or in pre-registration before a more complex transform is applied [27].

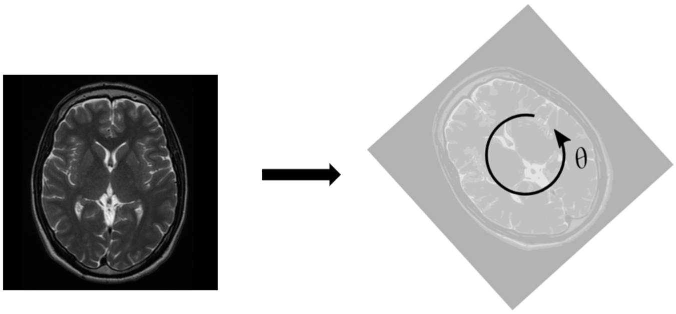

Figure 2.4: The concept of rigid transformation.

Affine Transformation

The affine transformation is a non-rigid model that allows translation, rotation, scaling and shear [27]. The function of scaling is to scale the set of points in each dimension respectively and shear offsets the set of points through a certain distance proportional to coordinates [28]. Figure 2.5 shows the concept of an affine transformation, with some rotation θ and scaling of the image. Regarding medical image analysis affine transformation is quite uncommon to use for the final image registration part, but as for with rigid transformation, it can be used in pre-registration of images [27].

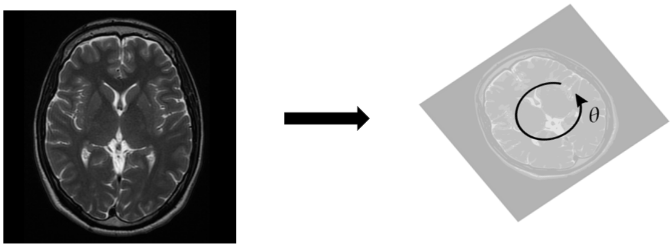

Figure 2.5: The concept of affine transformation.

Deformable Transformation

Medical image registration approaches are mostly based on curved transformations, as deformable transformation. This because almost all anatomical parts and organs of the human body are deformable structures [27].

To determine the deformation, many deformation models uses a grid of control points, which are considered as parameterised deformation models [27]. These points are moved individually in the direction that optimises some similarity metric, defining local deformations. The transformation between control points is then propagated by interpolation. Then, there is also non-parameterised, or so called dense deformation methods. When utilising dense deformation can each point in the moving image be displaced arbitrarily. This implies that there is a separate displacement vector stored for each voxel in the image [2]. In the case of deformable registration where the transformation is defined in the most general case, the transformation T at every voxel position x is given as the addition of the identity mapping and a displacement field u [29][2],

$$T(x) = x + u(x). \tag{2.6}$$

Figure 2.6 shows the concept of a non-parameterised deformable transformation, with arrows showing the deformation.

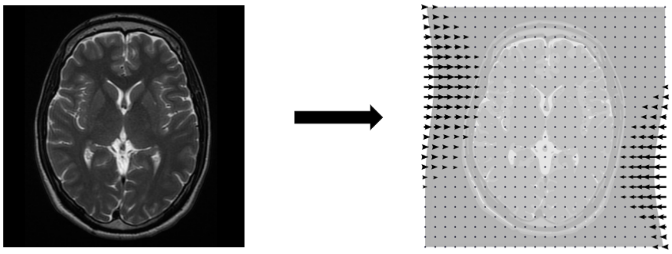

Figure 2.6: The concept of non-parameterised deformable transformation.

It is of importance to preserve the topology of the structures represented in the images to be registered [27]. The geometric transformation needs to be a invertible and differentiable mapping with differentiable inverse, which is a diffeomorphism [30]. Diffeomorphic image registration methodologies are know as those methodologies that use diffeomorphic transformations [27].

2.3.2 Similarity Metrics

The purpose of similarity metrics is to measure the similarity between images in the image registration process [28]. The higher the similarity after registration, the better the registration method performs. The sum of squared distances (SSD) is one metric which involves computation of the squared differences of the corresponding pixels in the two registered images [28]. The goal using SSD is to minimise its value, to achieve the best alignment between images. The SSD can be formulated as,

$$SSD = \sum_{v \in V_R} \left| R(v) - M_{T(v)} \right|^2 \tag{2.7}$$

where R is the reference image, M moving image, T transform and v corresponds to a voxel in the image space V_T [2]. Mutual information (MI) is another metric which is a basic concept from information theory [31]. MI in image registration is used to measure the amount of information that one image contains about the other

[31][32]. In contrast to SSD, the MI should be maximised, and when MI is maximal the images are optimally aligned. Additionally there is cross-correlation (CC), which estimates to which degree two images are correlated [33]. For the reference image R, moving image M and its transformed image M', the CC can be formulated as,

$$CC(R, M') = \frac{\sum_i (R(v) - \bar{R})(M'(v) - \bar{M}')}{\sqrt{\sum_i (R(v) - \bar{R})^2 \sum_i (M'(v) - \bar{M}')^2}} \tag{2.8}$$

where v is the voxel in the image where $v \in V_R$ and $\bar{R}$ and $\bar{M}'$ corresponds to mean values [33]. It is based on the assumption that there is a linear relation between the intensities of the corresponding structures in both images [27]. Consequently, the larger the cross-correlation is between reference and transformed image, the better the registration is. Then there is normalised cross-correlation (NCC) which originates from CC but where both the template and the image neighbourhood are suitably normalised [34].

2.3.3 Optimisation

The optimum regarding image registration corresponds to the transform that optimally registers the two input images [27]. The goal for the optimisation algorithm used is to search for the maximum or minimum value of a similarity metric, depending on which metric used. The similarity metrics are often defined so that the optimal registration is reached when their value is minimised [27]. It should be noted that for registration, there is no finite optimal solution. The registration problem can then be described as to find the transformation that optimises some similarity measure.

A coordinate mapping that relates two images is found using an iterative optimisation procedure [35]. The method of gradient descent optimisation is based on gradients and which assumes that the gradients can be calculated precisely. Gradient descent takes, with some step size, steps in the direction of the negative gradient of a function, the similarity metric.

Another approach for optimisation in image registration is to use move-making algorithms, which can for example be formulated as a discrete labelling problem [2]. The move-making algorithms starts with an initial solution, and then iteratively seeks to find better solutions. For each iteration, the algorithms are limited to a subset of the combinatorial search space, the move-space, and selects the one that gives the largest reduction to some objective function. The objective function f often consists of a data term and a regularisation term. It can be formulated as,

$$f(u) = (1 - \alpha)D + \alpha R \tag{2.9}$$

where u is the displacement field, α regularisation weight, D data term and R regularisation weight [2]. The data term corresponds to a measure of resemblance between the two registered images, which is the similarity metric, and the regularisation term enforces the smoothness of the deformation field itself. The regularisation term, or penalty, imposes a cost on the optimisation function, to make the optimal solution unique. The iterative method is terminated when the algorithm no longer can find an improving solution. This can be described as when,

$$f(u') < f(u) + \epsilon \tag{2.10}$$

where u is the displacement field, u' is the updated displacement field and ϵ is the block energy. The iterative method is stopped when there is no solution u' that gives a decrease in the objective function. The block energy is some small value that is used for tolerance within the optimisation. The move-making algorithms will converge in a finite number of steps, as long as the move-space holds the current solution. This gives that the resulting solution is guaranteed to be locally optimal, while there is no better solution existing within the move-space of the current solution.

The task of the registration algorithm is to estimate the optimal displacement field given the reference and moving image, where the optimisation problem can be described as,

$$u' = arg\underset{u}{min} f(u) \tag{2.11}$$

where u corresponds to the displacement field and f is the objective function [29].

An example of a move-making algorithm is the iterated conditional modes (ICM) method. It seeks to improve the current solution by iteratively changing the label of a single element at a time, while keeping all others fixed [2]. This means a small move-space, which makes the ICM prone to getting stuck in poor local minima. Another example of a move-making algorithm is α-expansion, which is used in graph-cut based optimisation. The algorithm selects a label α, and takes into consideration the available moves that allow all elements to either keep their current label or change label to α [36]. This algorithm has a much larger move-space, compared to the ICM method and then less prone to getting stuck in local minima [2]. The ICM seeks the local optimum per voxel, while the α-expansion with graph-cuts finds the global optimum for the whole image space. The disadvantage of using α-expansion however, is the high computational cost, which also increases non-linearly with image size and limits the use of α-expansion of large volume images.

Optimisation algorithms that are iterative are often implemented with a multi-resolution or pyramidal strategy [27]. This approach is initiated by registering the larger coarse structures and then transitions to the smaller details of the images. By defining a pair of image pyramids that are used to down-sample the reference and moving image, it registers the images from the lower to the higher resolution images. For each step, the transformation found in the previous step is used as a new initial registration. In comparison to methods that only uses the original images, this approach has some advantages with higher convergence radius, more robust to local optimums and is often faster [27].

Figure 2.7 shows a flow chart of a optimisation approach within the image registration process. For each iteration, the moving image is transformed and then compared to the reference image by the similarity metric. Then, the transformation model is updated by chosen optimisation approach and then the process starts over for the next iteration.

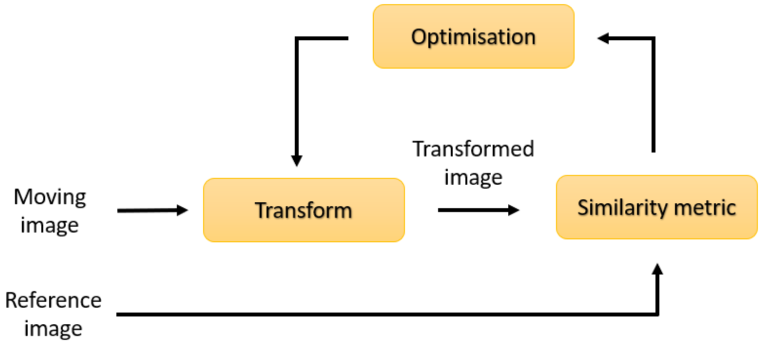

Figure 2.7: Flow chart for the optimisation process of image registration used in this method.

2.3.4 Fast Graph-Cut Based Optimisation

A method that implements deformable transformation is fast graph-cut based optimisation for practical dense deformable registration of volume images [2]. The presented method is formulated as a discrete labelling problem, with the focus on the optimisation methods of move-making algorithms. More specifically, dividing image space into overlapping sub-regions and restricting α-expansion moves to a single sub-region at a time [2]. By dividing the image into smaller sub-regions and then only modifying the displacement vectors within one region at a time, the computational cost can be reduced drastically [37]. The process per sub-region includes, constructing the graph by computing a voxelwise matching criterion and determines the optimal move by solving a minimal graph cut problem. This has been shown to only give a small decrease in quality of the solution. The presented method is specifically shown to work well for whole-body MR images [2].

2.3.5 Evaluation Metrics

Evaluation of the image registration is an important step for any use of image registration process. It is essential for evaluating different methods and parameters to understand how the registration and transformation affect the images, and if the methods are suitable for the task. However, the evaluation process comes with challenges since no ground truth of the transformed images exists.

Three important measures related to image registration are accuracy, reliability, and speed. Determining the accuracy requires that the results produced by the software are compared with true results. In this case, there is no known ground-truth, so for this reason intermediary metrics has to be used in an attempt to quantify the accuracy. One way to evaluate the accuracy is to use spatial overlapping metrics, further described in the next section. Reliability measures the software's ability to register images with varying degrees of noise, geometry and intensity. Lastly, speed is related to the computational load and the time it takes to perform the registration, which is of high importance for large scale analysis. [38]

Spatial Overlap Metric

The Dice Similarity Coefficient (DSC) is a spatial overlap based metric that is commonly used for medical image segmentation [27][32][39]. Dice measures the overlap between two sets and is calculated using the following equation,

$$\mathrm{DSC} = \frac{2|A \cap B|}{|A| + |B|} \tag{2.12}$$

where A and B are two sets of images that are compared. Possible Dice values range from zero to one, where one represents a total overlap and zero no overlap. The Dice is only for the regions being measured, for example the fat and water masks. Therefore, regions outside of the mask do not effect the evaluation, even though they might effect the transformation. Further, Dice is very dependent on the size of the regions, meaning a single voxel error can have a huge error for a smaller region. [40]

Transformation Evaluation

The transforms can also be used for evaluation of the image registration. To complement the overlap metrics various calculations can be made on the displacement field. Two examples are to calculate the magnitude and Jacobian determinant (or so called Jacobian) of the displacement field. The Jacobian can be described as the voxelwise change of the volume as an effect of the transformation. Plots of these calculations can then be observed to see if they appear realistic and where the transformation has found motion.

An additional way to evaluate the transformation is to determine whether it is diffeomorphic, previously explained in section 2.3.1. The Jacobian of the displacement field can be used for this, where a negative value indicates so called foldings in the displacement field. By calculating the number of voxels with values below zero, it can therefore be evaluated how diffeomorphic the transformation is [30]. Figure 2.8 shows two examples of a displacement field, where the one to the left shows a smooth transform and the right shows a folding. [30]

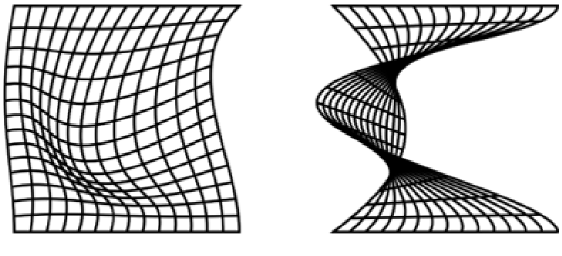

Figure 2.8: Illustration of folding in the Jacobian determinant in the right image, and a smooth displacement field to the left.

2.3.6 Motion Correction

Motion correction is applied to compensate for movements that has occurred during a scan. Correctly implemented motion correction can improve image quality and information accuracy. Motion correction can be implemented at different stages in the data processing, such as during or after image reconstruction. The correction can focus on different types of motion, where some were introduced in section 2.2. [1]

The development of hybrid PET/MR scanners has opened for the possibility to measure motion with both PET and MR imaging simultaneously. A previous motion correction method that has been implemented in PET/MR datasets is rigid-body motion correction [5]. It has been implemented for head motion and shows promising results. However, the assumption of a rigid-body motion may not work as well for other parts of the body. Moreover, other studies have implemented motion correction before or during reconstruction [6][7].

Motion correction for bulk motions have also been introduced in total-body PET/CT [41]. The method parameterise motion fields in-between neighbouring frames. The method was implemented in PET/CT and showed effective reduction of random body movements. A total-body PET/CT often provides the anatomical reference CT image once, compared to PET/MR where the PET and MR are acquired simultaneously.

Although, for already reconstructed datasets without access to the the raw data, only methods that apply motion correction post-reconstruction is applicable. There are also methods applying motion correction using only PET data [24]. However, then there is no anatomical reference such as when using MR or CT, and the PET scanner also provides limited spatial resolution. Furthermore, motion correction with only PET is also complicated due to the small amount of measured data from each position [1].

3

Methods

In the following chapter, the hybrid PET/MR dataset is introduced and the method is described. This regards both image registration of MR images, transforming PET images and modelling with Patlak. All experiments and evaluation were done using Python version 3.8. The general idea of the method is shown in figure 3.1. The motion is estimated between the MR images, to get a transformation, which then is applied to the corresponding PET images.

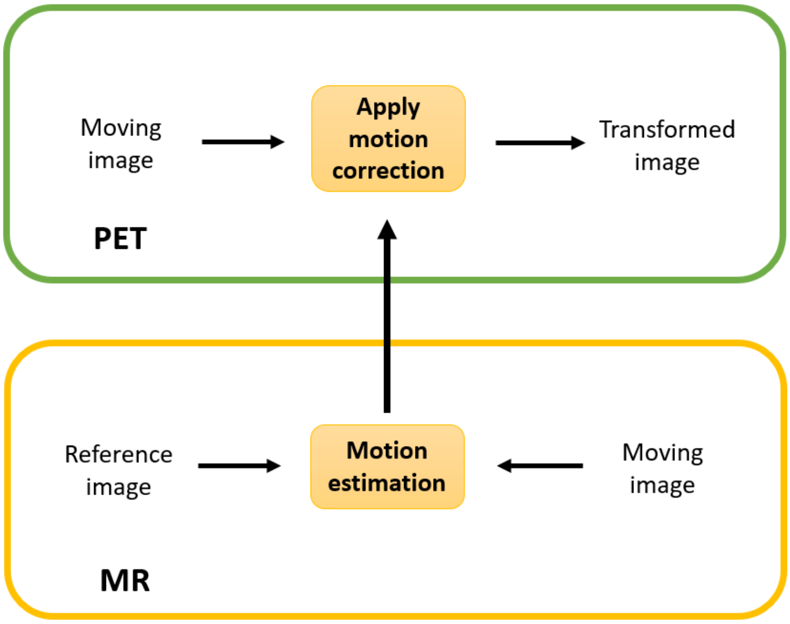

Figure 3.1: General flow chart of method.

3.1 Hybrid PET/MR Dataset

The dataset used in this study consists of 32 sets of dynamic whole-body PET and MR images. The protocol for the original dataset was initialised with a 10 min dynamic PET scan of the thorax. The protocol was continued with five whole-body PET/MR scans, with 30 s/bed, starting at average 15 min after FDG injection. The whole-body PET/MR scans was completed at average 60 min after FDG injection. This study uses the five time points with whole-body PET/MR images. The acquired MR images are of both water and fat, separately. The MR images are

MR-based Attenuation Correction (MRAC), meaning they have a lower resolution compared to normal MR imaging. The 32 different sets are of 16 subjects, with two visits each.

The dataset was already reconstructed and in DICOM format, pseudonymised and randomly sorted. All metadata unrelated to the quantification of PET was removed. It was known that the dataset contains movements between the time points, by varying degrees. The dataset was divided into training and test datasets, where 22 sets were randomly chosen for training and the remaining ten sets for testing. This is to prevent overfitting of the data. A good result for training data does not guarantee the success of the method on other data. The division allowed for an accurate evaluation of the method by testing it on the designated test data. Of the five time points per set, the fifth time point was chosen as the reference image and the rest are referred to as moving images. Note that the term moving image refers to the image that is compared to the reference image, and not that the image itself is moving. It should also be noted that the segmentations for water and fat were made on the reference images.

3.1.1 Ethical, Ecological and Social Aspects

Regarding the ethical aspects of this study, the used material is from a previous clinical study that was approved with an ethical permit and informed consent from all participants involved. No new dataset was acquired. The dataset used is anonymised and secured to remain integrity of the participants, following the policies of Good Clinical Practice (GCP). Mandatory training for GCP and personal data protection was required prior to access and analysis of the clinical datasets.

For the ecological aspects, as previously stated, this study uses already existing data which does not have any ecological impact. For the social aspects, this work will be carried out in a healthcare area and the solution found via this work could potentially improve future studies that use this type of methodology. Further, more accurate measurements could decrease the number of subjects that is needed in clinical trials using this type of methods, and thereby fewer subjects exposed to radiation.

3.2 Implementation of Registration Method

In this section the different steps in the used registration method is presented. This regards pre-processing of data, pre-registering images and the main part of the method with deformable image registration. Note that the implementation of the registration method is done on the MR images, and optimisation of the parameter settings was only done on the training data.

3.2.1 Pre-Processing

The MR images in the dataset was initially converted from DICOM to NRRD format. Pre-processing of the images was then firstly done by clamping data to 0.01 and 0.99 percentiles, to reduce noise. Then it was normalised to $0-1$.

3.2.2 Pre-Registration

After pre-processing of data, a pre-registration was performed on the images. It was done with an internal tool that uses SimpleITK v2.2.1 in python [42]. This was done by utilising a two step process with an initial rigid registration followed by an affine registration. Note that the affine registration was optional and some tests were done using only rigid transformation. Other parameters used in the pre-registration were set as default. The registration was performed between the four moving images in each set to its reference image separately. In the pre-registration, a mutual information similarity metric was used along with gradient decent for optimisation.

3.2.3 Deformable Registration

The main part of the image registration method was done with deformable image registration. With the $pydeform$ package in python, fast graph-cut based optimisation was utilised for the registration [2][43]. Optimisation with move-making algorithms and the similarity metric used was normalised cross correlation. All deformable registration was done with the use of GPU. Fixed parameter settings used which are suitable for large volume MR images are presented in table 3.1 [2]. Update rule regards the update of the displacement field, and an additive update rule gives that the displacement is added for each iteration. The parameter called block is the size of the sub-region and block energy corresponds to the limit for accepted solution within the optimisation step. The registration was then performed, as in pre-registration, between the four moving images in each set to its reference image separately.

Table 3.1: Fixed parameter settings for deformable registration.

Parameter	Setting
Update rule	additive
Block	[16, 16, 16]
Block energy	$\epsilon = 1e - 7$

3.3 Evaluation of Image Registration Method

The image registration was evaluated in multiple steps, such as applying segmentations and using evaluation metrics (introduced in section 2.3.5), and is described in the following section.

3.3.1 Segmentations

A part of the image registration evaluation process was to create fat and water segmentations of the MR data. Note that these segmentations are not the same as the tissue segmentations used for the PET images. The water and fat segmentations were used to calculate the Dice score for the them separately, and also for merged segmentations. Automatic segmentations of fat and water was previously performed with an internal software based on a fuzzy c-means clustering method [44]. The segmentations were then manually adjusted in SmartPaint [45]. The segmentations were made to the reference MR images of all sets in the dataset. The adjustments included the removal of artifacts and the arms, starting from a straight line up from the armpit. The arms were removed due to the datasets' inconsistency of how much of the arms were in the images. For some images there were only some parts of the arms visible. Other adjustments to the segmentations were the removal of medical equipment, such as intravenous tubes.

3.3.2 Phase 1

An initial evaluation was performed to understand how the parameters interact. For this phase where the parameter settings set to cover a relatively wide range of combinations. The main evaluation metrics used in this phase was Dice score and computational time, with the aim to find the most promising setup range of parameters. This regards minimum level of pyramid, number of iterations, step size, regularisation weight and choice of of transformation in pre-registration.

The start of phase 1 was to evaluate the minimum pyramid level as well as using affine or rigid transformation in the pre-registration. Testing with rigid transformation were only performed on settings with 20 iterations and minimum pyramid level set to 1, otherwise all possible combinations were tested, which are shown in table 3.2. Furthermore, for the tests with rigid transformation was only image 1 and 3 in every set to shorten run time. In total, 36 different affine transformation parameter combinations and 9 rigid transformation parameter combinations were tested for this phase.

Table 3.2: Parameter setting options for initial testing.

Parameter	Settings
Transformation (pre-reg.)	Rigid, Affine
Minimum pyramid level	1 (only affine), 2
Number of iterations	10 (only affine), 20
Step size	0.1, 0.3, 0.5
Regularisation weight	0.05, 0.15, 0.25

3.3.3 Phase 2

For this phase, the main focus was on the interaction between step size and regularisation weight. The parameter setups for this phase were chosen after evaluating the more promising parameter settings from phase 1. The parameter values chosen are shown in table 3.3 and all possible combinations of these were tested, resulting in 20 combinations. The main evaluation metrics were Dice score and the ratio of zeros in the Jacobian determinant, as well as visualisation of the magnitude of the displacement field to investigate outliers.

Table 3.3: Parameter setting options for first optimisation.

Parameter	Settings
Transformation (pre-reg.)	Affine
Minimum pyramid level	1
Number of iterations	10
Step size	0.05, 0.075, 0.1, 0.15
Regularisation weight	0.01, 0.03, 0.05, 0.07, 0.1

3.3.4 Phase 3

This phase was performed to investigate an increased number of iterations for the smaller step sizes and regularisation weights. Similarly to the previous phase, the evaluation metrics used were Dice score and the ratio of zeros in the Jacobian determinant. The chosen parameter values are presented in table 3.4.

Table 3.4: Parameter setting options for second optimisation.

Parameter	Settings
Transformation (pre-reg.)	Affine
Minimum pyramid level	1
Number of iterations	10, 20
Step size	0.05, 0.075, 0.1
Regularisation weight	0.01, 0.03, 0.05

3.4 Validation of Image Registration Method

The validation of the image registration method was done after the optimisation on the training dataset was concluded. Running registration for the test data was done with a range of the most promising parameter setups from phase 2, which are shown in table 3.5. Note that no optimisation of parameters was based on the results from the test data. A range of parameter settings was wanted rather than one single specific setting. This, due to the fact that the dataset is relatively small and the most optimal parameter setup may vary to some extent between different datasets.

Table 3.5: Parameter setting options for validation.

Parameter	Settings
Transformation (pre-reg.)	Affine
Minimum pyramid level	1
Number of iterations	10
Step size	0.05, 0.075, 0.1
Regularisation weight	0.05, 0.07, 0.1

3.5 Motion Correction on PET Data

The motion correction was performed by applying transformations on the PET images, where the transformations where the result from the method of image registration with the MR images. To analyse the effect of motion correction on the PET readouts, multiple segmentations of different tissues were used. The segmentations of tissues were created prior to this work, using an in house developed and validated semi-automated segmentation programme and the *PMOD* software v4.204 (PMOD Technologies LLC, Zurich, Switzerland). This was done for each PET reference image (the last time point) of all sets in the dataset. The segmentations made were brain, liver, pancreas (panc), left quadriceps femoris muscle (lquad), right quadriceps femoris muscle (rquad), myocardium (myoc), subcutaneous adipose tissue (sat) and visceral adipose tissue (vat). Figure 3.2 shows an overview of the different segmentations, with a coronal slice of a fused PET and MR image.

The parameter settings of the transformations used for motion correction of the PET images were the same as the ones presented in table 3.5. A transformation was applied on the first four PET images in each set and then evaluated with the different segmentations.

3.5.1 Evaluation of Motion Correction

For the evaluation of motion correction on the PET data, the data set was divided into two groups, sets with and without motion in the segmented areas. The division was decided based on original fat and water Dice score for the MR data. Sets with either fat or water Dice score lower than 0.56 were chosen for manual inspection of the motion. These are shown in table A.1 in appendix A.1. The sets with artifacts affecting the Dice score, or motion in areas outside of the PET segmentations (e.g. feet) were placed in the group without motion. The remaining sets with low Dice score were placed in the group of sets with motion. There were twelve sets with Dice below 0.56, whereof four with artifacts, three with motion outside of segmentations and then five left for the group with motion.

To evaluate the effect on the PET readouts, the Patlak model was used to calculate the K_i values and its RSE (the goodness of the Patlak fit) for all segmentations in each set. These calculations were also made on all sets without transformation, to use as reference. This was used to evaluate the possible difference between sets with and without motion, as well as for the effect in different segmentations. Besides the calculations from the Patlak modelling, visual evaluation was also used to observe the effect on different segmentations.

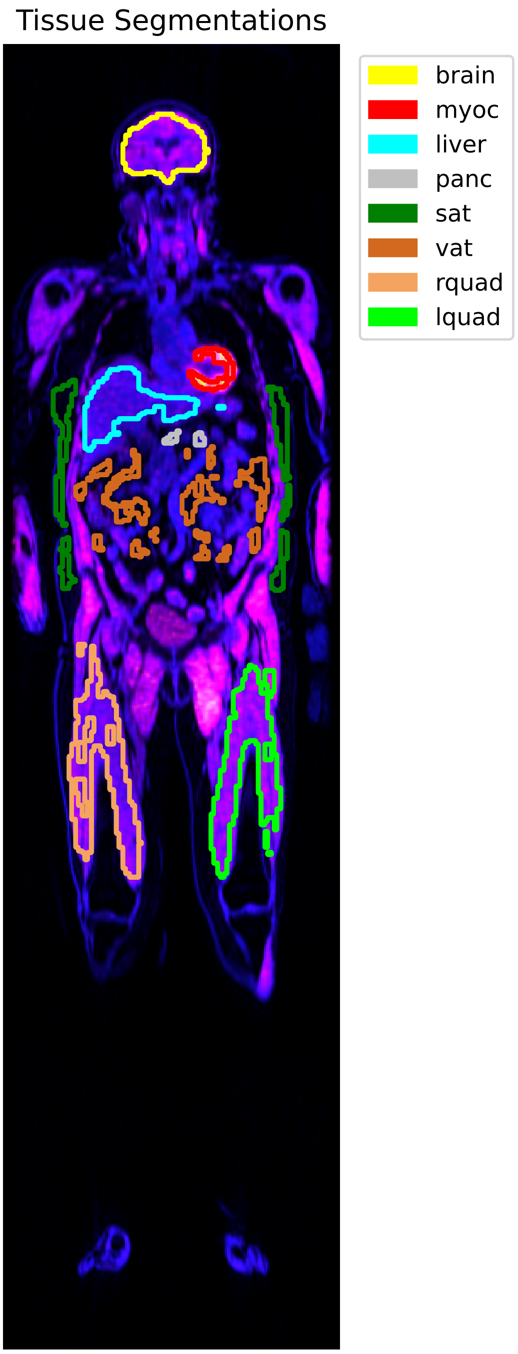

Figure 3.2: Overview of tissue segmentations, brain, liver, pancreas (panc), left quadriceps femoris muscle (lquad), right quadriceps femoris muscle (rquad), myocardium (myoc), subcutaneous adipose tissue (sat) och visceral adipose tissue (vat).

4

Results

In the following chapter, the results are presented for image registration of MR images and the impact onto the PET readout of the motion corrected PET images. The image registration part consists of the results from implementation of fast graph-cut optimisation in terms of Dice scores, zeros in Jacobians and magnitude plots. Regarding applying motion correction on the PET data, it was done with the more promising parameter setups from the image registration part. These results consists of K_i values from Patlak plots along with RSE values.

4.1 Image Registration of MR Images

The following section is divided into training data and test data, where the evaluation is presented respectively. The results regarding training and test data is presented with scatter plots, heatmaps and box plots. Tables with all mean scores as well as standard deviation is also presented. Furthermore, this part of the results is finalised with a section regarding the visual interpretation.

4.1.1 Training Data

The results of the training data is presented for each phase, 1, 2 and 3. Phase 1 presents the results of setting options for choice of pre-registration transformation, pyramid levels and also for different number of iterations, step sizes and regularisation weights. For phase 2 and 3, the pre-registration transformation and pyramid levels were fixed and presents results for varying step sizes and regularisation weights. Note that the number of iterations was fixed for phase 2, but not for phase 3.

Phase 1

For the choice of pre-registration transformation, evaluation comparing rigid and affine transformation was performed. A scatter plot with the mean Dice score and run time regarding the parameter combinations (presented in table 3.2) is shown in figure 4.1. Each point corresponds to the mean dice and run time for all sets in the training data, for one parameter setting. Note that only time point 1 and 3 for every set are used in this plot. The figure shows that rigid and affine performs similarly in regards to both Dice score and run time. The mean run time is the mean time for registering and creating a transformation for one time point in a set, and does not include additional processing of the produced transform.

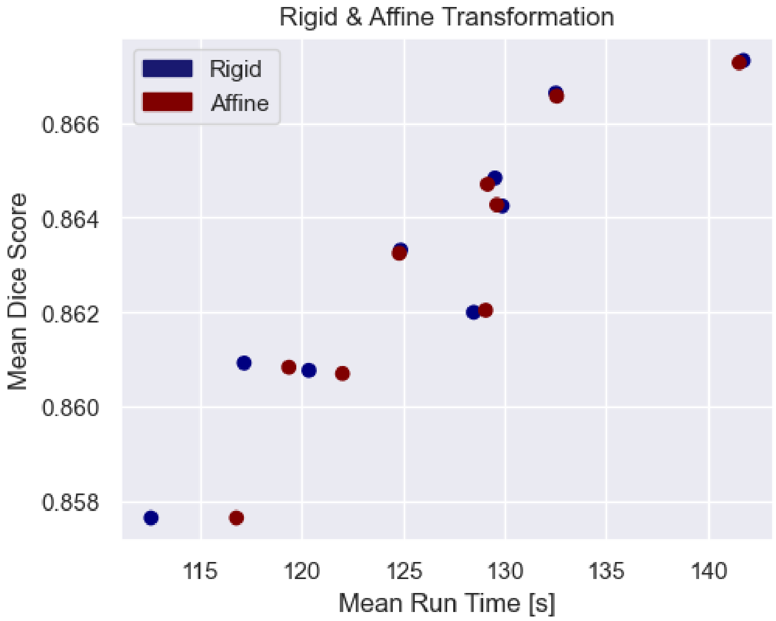

Figure 4.1: Scatter plot comparing rigid and affine transformation, used in pre-registration. For parameter setting options in phase 1.

Figure 4.2 shows a comparison of pyramid level and number of iterations. Each point corresponds to the mean dice and run time for all sets and all time points in the training data, for one parameter setting. Four clusters can be identified from the figure, related to the four combinations of these two parameters. Minimum pyramid level 1 results in higher Dice score than level 2, but also shows longer run times. Regarding number of iterations, it can be seen that both 10 and 20 iterations results in similar Dice score. However, 20 iterations results in a longer run time, where the difference is larger for minimum pyramid level 1 than level 2.

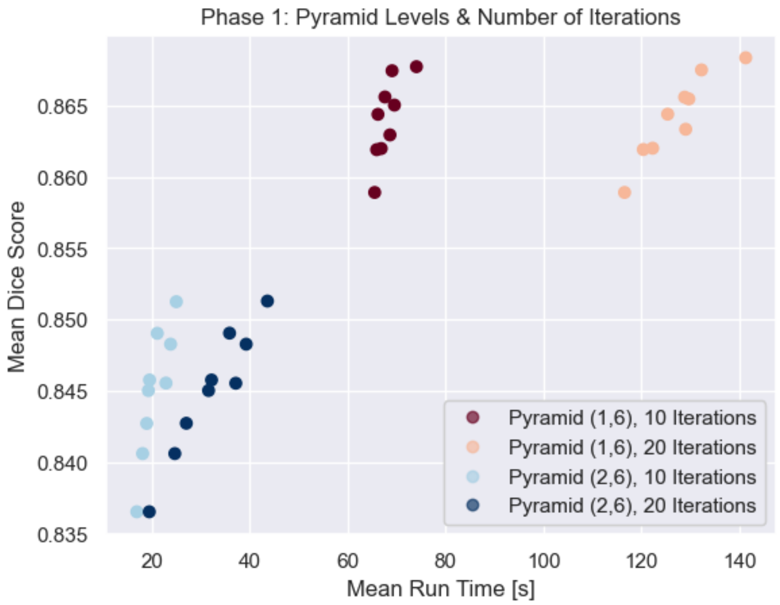

Figure 4.2: Scatter plot comparing pyramid levels and number of iterations. For parameter setting options in phase 1.

Mean Dice scores and run times for phase 1 is shown in table 4.1, which regards all pyramid levels, number of iterations, step sizes and regularisation weights. Note that the values presented in the table is for affine transformation in pre-registration. Now, with pyramid level set to (1,6), 10 iterations and affine transformation in pre-registration, results for different step sizes and regularisation weights is shown in figure 4.3 and 4.4. The first, presenting a heatmap of mean Dice scores for the different parameter setups for MR water images and the second for MR fat images.

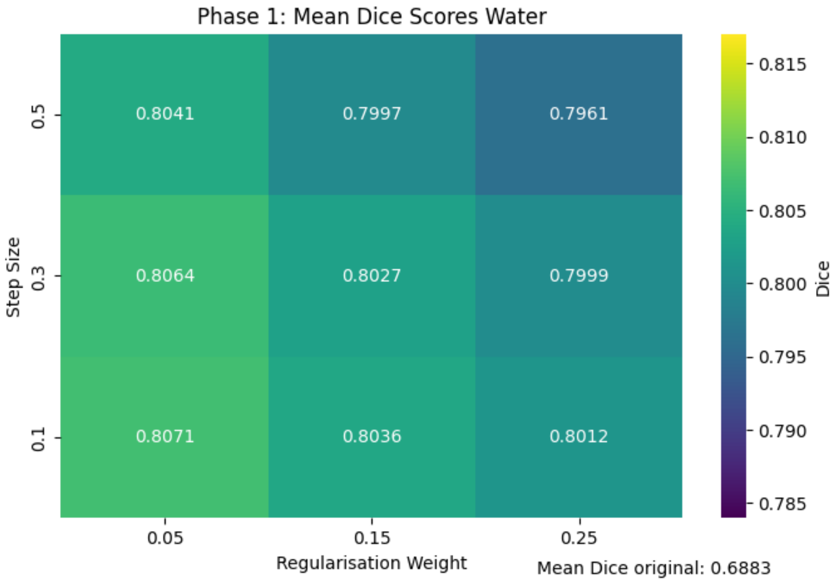

Figure 4.3: Heatmap of mean Dice scores for MR water images. Pyramid levels (1,6), 10 iterations, affine transformation i pre-registration.

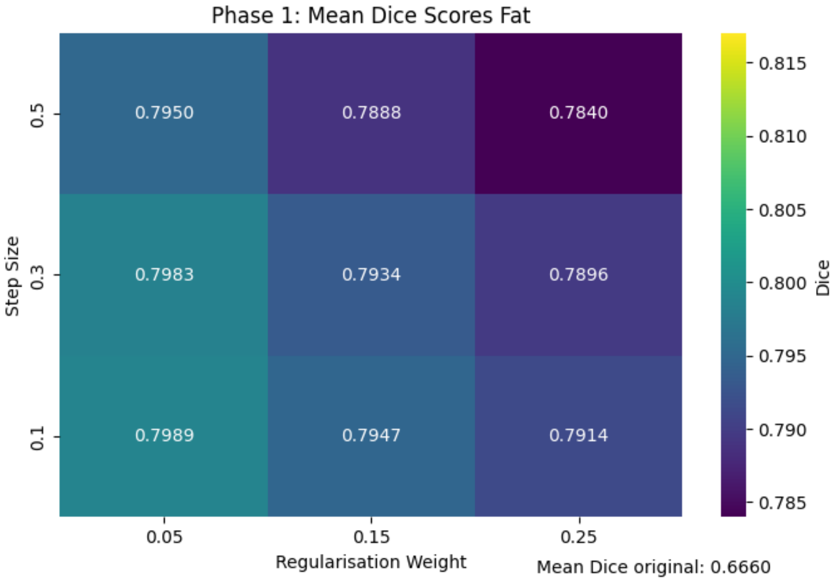

Figure 4.4: Heatmap of mean Dice scores for MR fat images. Pyramid levels (1,6), 10 iterations, affine transformation i pre-registration.

Table 4.1: Dice scores for water, fat and merged, all for segmented images. Dice scores for the original images are for water 0.6693, fat 0.6408 and merged 0.7685.

Parameter Setup				Run	Dice Scores					
Affine pre-reg.				Time	Mean			std		
Pyr.	Iter.	Step.	Weig.	Mean [s]	W	F	M	W	F	M
(1,6)	10	0.1	0.05	74	0.807	0.799	0.868	0.061	0.074	0.035
(1,6)	10	0.1	0.15	69	0.804	0.795	0.865	0.061	0.076	0.036
(1,6)	10	0.1	0.25	68	0.801	0.791	0.863	0.061	0.077	0.036
(1,6)	10	0.3	0.05	69	0.806	0.798	0.867	0.061	0.074	0.035
(1,6)	10	0.3	0.15	66	0.803	0.793	0.864	0.061	0.076	0.035
(1,6)	10	0.3	0.25	66	0.800	0.790	0.862	0.061	0.077	0.035
(1,6)	10	0.5	0.05	67	0.804	0.795	0.866	0.061	0.074	0.035
(1,6)	10	0.5	0.15	65	0.800	0.789	0.862	0.061	0.076	0.035
(1,6)	10	0.5	0.25	65	0.796	0.784	0.859	0.061	0.078	0.035
(1,6)	20	0.1	0.05	141	0.808	0.800	0.868	0.061	0.074	0.035
(1,6)	20	0.1	0.15	129	0.804	0.795	0.865	0.061	0.076	0.035
(1,6)	20	0.1	0.25	129	0.802	0.792	0.863	0.061	0.077	0.036
(1,6)	20	0.3	0.05	132	0.807	0.798	0.868	0.061	0.074	0.035
(1,6)	20	0.3	0.15	125	0.803	0.793	0.864	0.061	0.076	0.035
(1,6)	20	0.3	0.25	122	0.800	0.790	0.862	0.061	0.077	0.035
(1,6)	20	0.5	0.05	128	0.804	0.795	0.866	0.061	0.074	0.035
(1,6)	20	0.5	0.15	120	0.800	0.789	0.862	0.061	0.076	0.035
(1,6)	20	0.5	0.25	116	0.796	0.784	0.859	0.061	0.078	0.035
(2,6)	10	0.1	0.05	24	0.789	0.770	0.851	0.060	0.084	0.037
(2,6)	10	0.1	0.15	23	0.785	0.764	0.848	0.060	0.088	0.037
(2,6)	10	0.1	0.25	22	0.781	0.759	0.846	0.059	0.091	0.036
(2,6)	10	0.3	0.05	21	0.786	0.765	0.849	0.060	0.087	0.036
(2,6)	10	0.3	0.15	19	0.782	0.759	0.846	0.060	0.091	0.036
(2,6)	10	0.3	0.25	18	0.778	0.754	0.843	0.059	0.092	0.036
(2,6)	10	0.5	0.05	19	0.781	0.758	0.845	0.059	0.089	0.036
(2,6)	10	0.5	0.15	18	0.775	0.752	0.841	0.060	0.091	0.037
(2,6)	10	0.5	0.25	16	0.771	0.746	0.837	0.058	0.093	0.037
(2,6)	20	0.1	0.05	43	0.789	0.770	0.851	0.060	0.084	0.037
(2,6)	20	0.1	0.15	39	0.785	0.764	0.848	0.060	0.088	0.037
(2,6)	20	0.1	0.25	37	0.781	0.759	0.846	0.059	0.091	0.036
(2,6)	20	0.3	0.05	35	0.786	0.765	0.849	0.060	0.087	0.036
(2,6)	20	0.3	0.15	32	0.782	0.759	0.846	0.060	0.091	0.036
(2,6)	20	0.3	0.25	27	0.778	0.754	0.843	0.059	0.092	0.036
(2,6)	20	0.5	0.05	31	0.781	0.758	0.845	0.059	0.089	0.036
(2,6)	20	0.5	0.15	24	0.775	0.752	0.841	0.060	0.091	0.037
(2,6)	20	0.5	0.25	19	0.771	0.746	0.837	0.058	0.093	0.037

Regarding parameter setup, Pyr. = pyramid, Iter.= number of iterations, Step. = step size and Weig. = regularisation weight. Regarding Dice scores, W = segmented water, F = segmented fat and M = merged segmentations of water and fat.

Phase 2

All mean Dice scores and run times for phase 2 is shown in table 4.2. Mean Dice scores is also shown in heatmaps for water and fat MR images in figure 4.5 and 4.6.

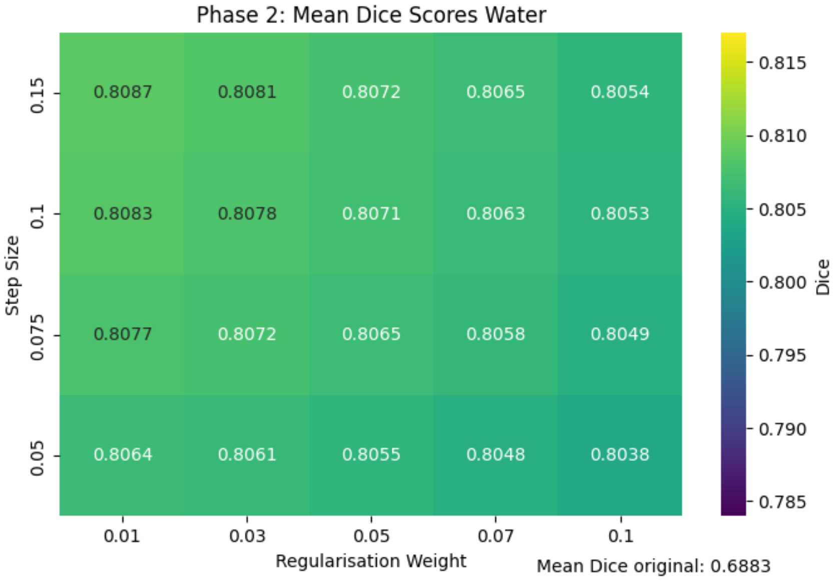

Figure 4.5: Heatmap of mean Dice scores for MR water images. Pyramid levels (1,6), 10 iterations, affine transformation i pre-registration.

Figure 4.6: Heatmap of mean Dice scores for MR fat images. Pyramid levels (1,6), 10 iterations, affine transformation i pre-registration.

Table 4.2: Dice scores for water, fat and merged, all for segmented images. Dice scores for the original images are for water 0.6693, fat 0.6408 and merged 0.7685. Number of iterations 10, pyramid levels (1,6) and affine transformation in pre-registration.

Parameter Setup		Run Time	Dice Scores					
			Mean			std		
Step.	Weig.	Mean [s]	W	F	M	W	F	M
0.05	0.01	76	0.806	0.798	0.867	0.062	0.074	0.036
0.05	0.03	76	0.806	0.797	0.867	0.062	0.075	0.036
0.05	0.05	76	0.805	0.797	0.866	0.062	0.075	0.036
0.05	0.07	75	0.805	0.796	0.866	0.062	0.075	0.036
0.05	0.1	74	0.804	0.795	0.865	0.062	0.076	0.036
0.075	0.01	76	0.808	0.800	0.868	0.061	0.073	0.035
0.075	0.03	75	0.807	0.799	0.868	0.061	0.074	0.036
0.075	0.05	74	0.807	0.798	0.867	0.062	0.074	0.036
0.075	0.07	74	0.806	0.797	0.867	0.062	0.075	0.036
0.075	0.1	73	0.805	0.796	0.866	0.062	0.075	0.036
0.1	0.01	75	0.808	0.800	0.869	0.061	0.073	0.035
0.1	0.03	75	0.808	0.800	0.868	0.061	0.074	0.035
0.1	0.05	74	0.807	0.799	0.868	0.061	0.074	0.035
0.1	0.07	73	0.806	0.798	0.867	0.061	0.075	0.035
0.1	0.1	71	0.805	0.797	0.866	0.061	0.075	0.035
0.15	0.01	75	0.809	0.801	0.869	0.061	0.073	0.035
0.15	0.03	74	0.808	0.800	0.869	0.061	0.074	0.035
0.15	0.05	72	0.807	0.799	0.868	0.061	0.074	0.035
0.15	0.07	71	0.806	0.798	0.867	0.061	0.074	0.035
0.15	0.1	69	0.805	0.797	0.866	0.061	0.075	0.035

Regarding parameters, Step. = step size and Weig. = regularisation weight. Regarding Dice scores, W = segmented water, F = segmented fat and M = merged segmentations of water and fat.

Regarding evaluation of the deformation field, a heatmap for mean zeros in Jacobian ratio is shown in figure 4.7. All values regarding the Jacobian is shown in table 4.3.

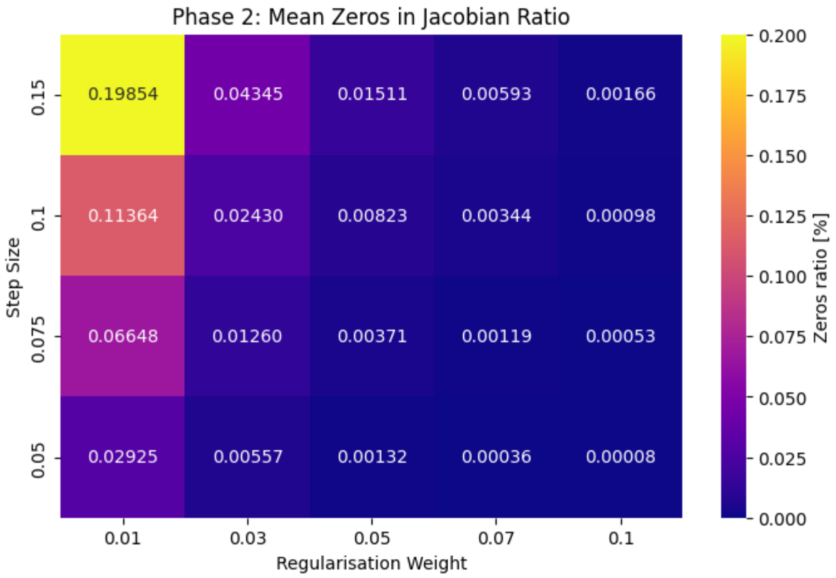

Figure 4.7: Heatmap of mean zeros in Jacobian ratio, with pyramid (1,6), 10 iterations and affine transformation in pre-registration.

A box plot for the zeros in Jacobian ratio of phase 2 is shown in figure 4.8. Regularisation weight 0.01 shows the largest amount of zeros for all step sizes. Some distinctive outliers can be identified.

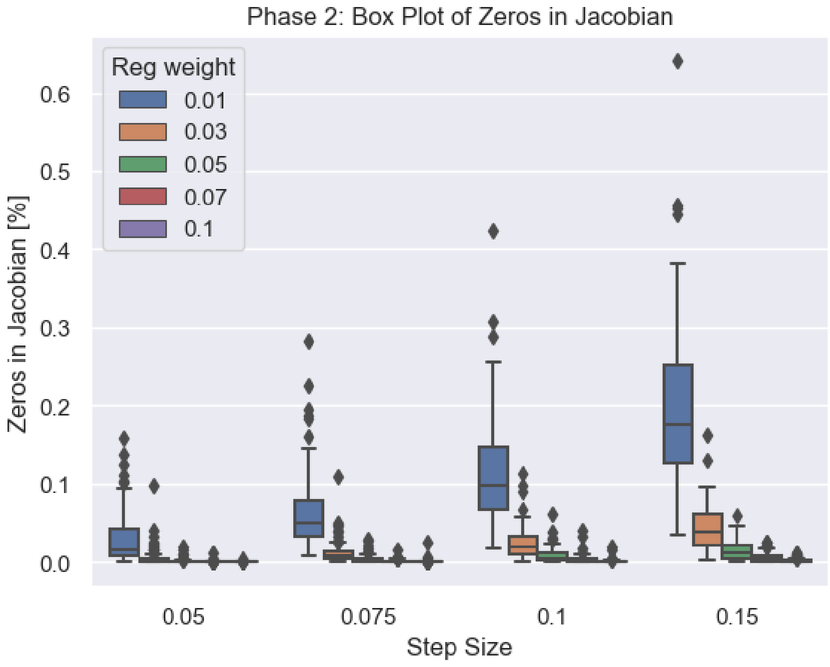

Figure 4.8: Box plot of the ratio of zeros in the Jacobian determinant, for the different parameter settings in phase 2.

Table 4.3: Scores for evaluating Jacobians. Number of iterations 10, pyramid levels (1,6) and affine transformation in pre-registration.

Parameters		Jacobian	
Step.	Weig.	Mean zero ratio [%]	Mean Jacobian
0.05	0.01	0.02925	0.14510
0.05	0.03	0.00557	0.14511
0.05	0.05	0.00132	0.14512
0.05	0.07	0.00036	0.14512
0.05	0.1	0.00008	0.14511
0.075	0.01	0.06648	0.14511
0.075	0.03	0.01260	0.14512
0.075	0.05	0.00371	0.14512
0.075	0.07	0.00119	0.14511
0.075	0.1	0.00053	0.14510
0.1	0.01	0.11364	0.14511
0.1	0.03	0.02430	0.14512
0.1	0.05	0.00823	0.14512
0.1	0.07	0.00344	0.14511
0.1	0.1	0.00098	0.14510
0.15	0.01	0.19854	0.14512
0.15	0.03	0.04345	0.14513
0.15	0.05	0.01511	0.14512
0.15	0.07	0.00593	0.14511
0.15	0.1	0.00166	0.14508

Step. = step size and Weig. = regularisation weight.

Phase 3

All mean Dice scores and run times for phase 3 is shown in table 4.4. Mean Dice scores is also shown in heatmaps for water and fat MR images in figure 4.9 and 4.10.

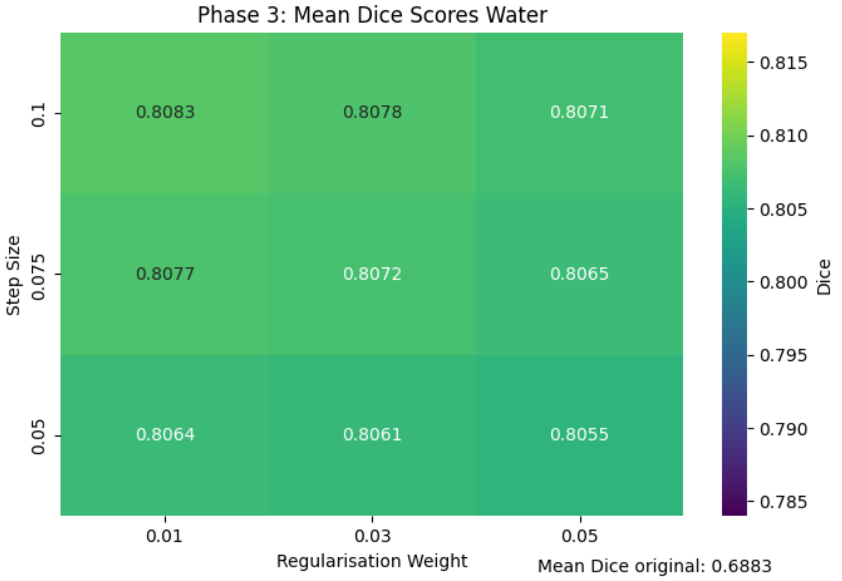

Figure 4.9: Heatmap of mean Dice scores for MR water images. Pyramid levels (1,6), 10 iterations, affine transformation i pre-registration.

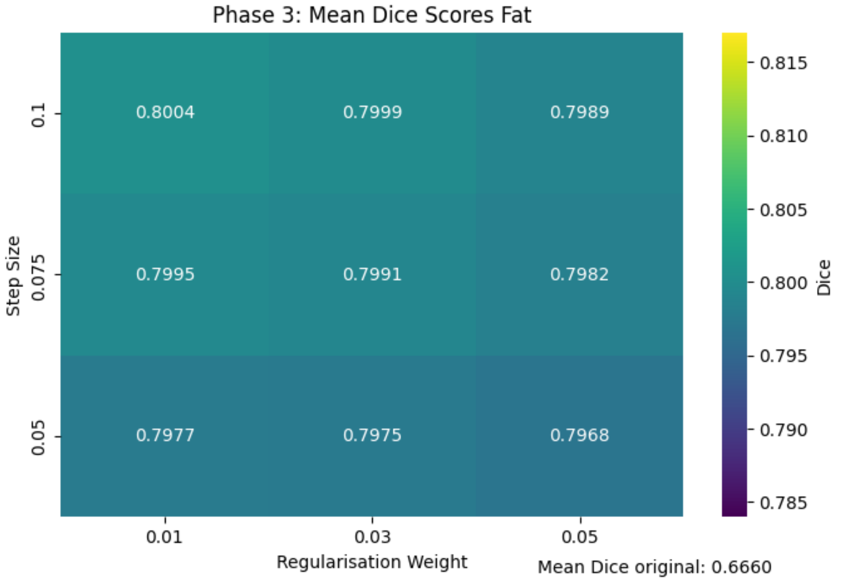

Figure 4.10: Heatmap of mean Dice scores for MR fat images. Pyramid levels (1,6), 10 iterations, affine transformation i pre-registration.

Table 4.4: Dice scores for water, fat and merged, all for segmented images. Dice scores for the original images are for water 0.6693, fat 0.6408 and merged 0.7685. Pyramid levels (1,6) and affine transformation in pre-registration.

Parameter Setup			Run Time	Dice Scores					
				Mean			std		
Iter.	Step.	Weig.	Mean [s]	W	F	M	W	F	M
10	0.05	0.01	76	0.806	0.798	0.867	0.062	0.074	0.036
10	0.05	0.03	76	0.806	0.797	0.867	0.062	0.075	0.036
10	0.05	0.05	76	0.805	0.797	0.866	0.062	0.075	0.036
10	0.075	0.01	76	0.808	0.800	0.868	0.061	0.073	0.035
10	0.075	0.03	75	0.807	0.799	0.868	0.061	0.074	0.036
10	0.075	0.05	74	0.807	0.798	0.867	0.062	0.074	0.036
10	0.1	0.01	75	0.808	0.800	0.869	0.061	0.073	0.035
10	0.1	0.03	75	0.808	0.800	0.868	0.061	0.074	0.035
10	0.1	0.05	74	0.807	0.799	0.868	0.061	0.074	0.035
20	0.05	0.01	148	0.809	0.801	0.869	0.061	0.073	0.035
20	0.05	0.03	147	0.808	0.800	0.868	0.061	0.074	0.035
20	0.05	0.05	145	0.807	0.799	0.868	0.061	0.074	0.035
20	0.075	0.01	146	0.809	0.802	0.869	0.061	0.073	0.035
20	0.075	0.03	146	0.808	0.801	0.869	0.061	0.074	0.035
20	0.075	0.05	143	0.808	0.800	0.868	0.061	0.074	0.035
20	0.1	0.01	145	0.809	0.802	0.870	0.061	0.073	0.035
20	0.1	0.03	144	0.809	0.801	0.869	0.061	0.073	0.035
20	0.1	0.05	141	0.808	0.800	0.868	0.061	0.074	0.035

Regarding parameters, Iter. = number of iterations, Step. = step size and Weig. = regularisation weight. Regarding Dice scores, W = segmented water, F = segmented fat and M = merged segmentations of water and fat.

Regarding evaluation of the deformation field, a heatmap for mean zeros in Jacobian ratio is shown in figure 4.11. Values regarding the Jacobian is shown in table 4.5.

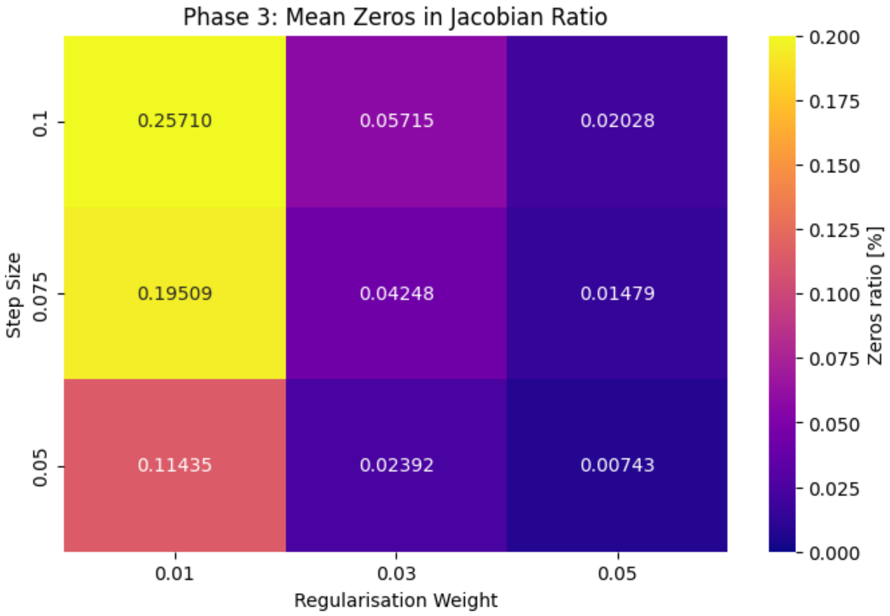

Figure 4.11: Heatmap of mean zeros in Jacobian ratio, with pyramid (1,6), 20 iterations and affine transformation in pre-registration.

Table 4.5: Scores for evaluating Jacobians. Pyramid levels (1,6) and affine transformation in pre-registration.

Parameters			Jacobian	
Iter.	Step.	Weig.	Mean zero ratio [%]	Mean Jacobian
10	0.05	0.01	0.02925	0.14510
10	0.05	0.03	0.00557	0.14511
10	0.05	0.05	0.00132	0.14512
10	0.075	0.01	0.06648	0.14511
10	0.075	0.03	0.01260	0.14512
10	0.075	0.05	0.00371	0.14512
10	0.1	0.01	0.11364	0.14511
10	0.1	0.03	0.02430	0.14512
10	0.1	0.05	0.00823	0.14512
20	0.05	0.01	0.11435	0.14511
20	0.05	0.03	0.02392	0.14512
20	0.05	0.05	0.00743	0.14512
20	0.075	0.01	0.19509	0.14512
20	0.075	0.03	0.04248	0.14512
20	0.075	0.05	0.01479	0.14512
20	0.1	0.01	0.25710	0.14512
20	0.1	0.03	0.05715	0.14513
20	0.1	0.05	0.02028	0.14511

Iter. = number of iterations, Step. = step size and Weig. = regularisation weight.

4.1.2 Test Data

In this section the registration results regarding the test data is presented. Figure 4.12 and 4.13 shows a heatmap of mean Dice scores for water and fat MR images. All mean Dice scores and run times for the test data is shown in table 4.6.

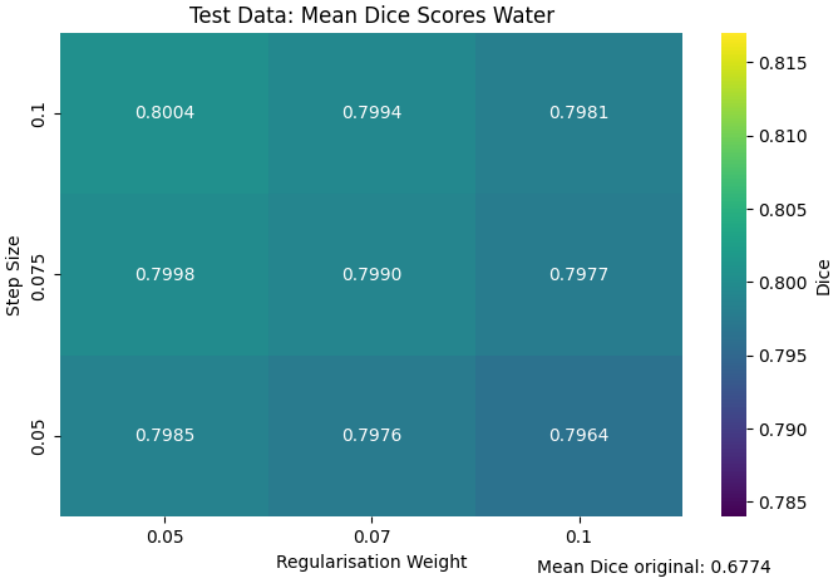

Figure 4.12: Heatmap of mean Dice scores for MR water images. Pyramid levels (1,6), 10 iterations, affine transformation i pre-registration.

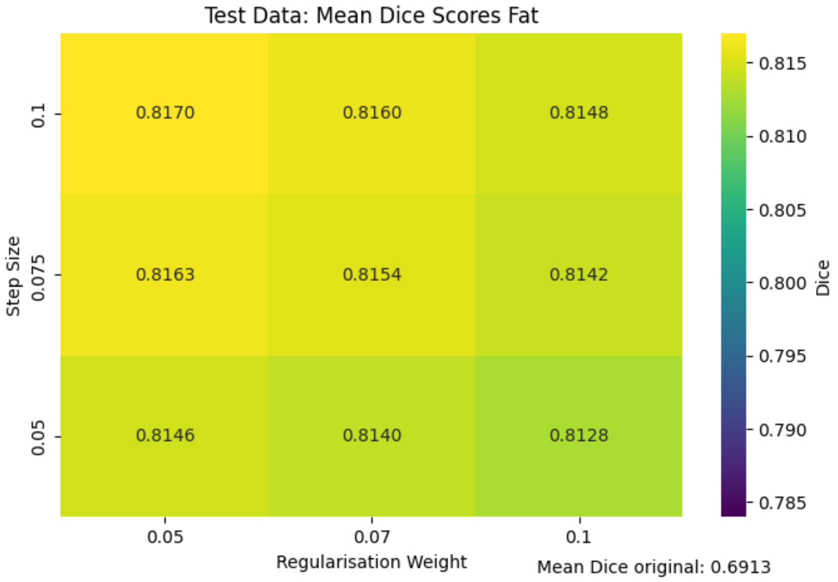

Figure 4.13: Heatmap of mean Dice scores for MR fat images. Pyramid levels (1,6), 10 iterations, affine transformation i pre-registration.

Table 4.6: Dice scores for water, fat and merged, all for segmented images. Dice scores for the original images are for water 0.6693, fat 0.6408 and merged 0.7685. Pyramid levels (1,6), 10 iterations and affine transformation in pre-registration.

Parameter Setup		Run Time	Dice Scores					
			Mean			std		
Step.	Weig.	Mean [s]	W	F	M	W	F	M
0.05	0.05	76	0.798	0.815	0.873	0.056	0.077	0.035
0.05	0.07	75	0.798	0.814	0.873	0.057	0.078	0.036
0.05	0.1	75	0.796	0.813	0.872	0.057	0.078	0.036
0.075	0.05	75	0.800	0.816	0.874	0.055	0.076	0.035
0.075	0.07	74	0.799	0.815	0.874	0.056	0.076	0.035
0.075	0.1	73	0.798	0.814	0.873	0.056	0.077	0.035
0.1	0.05	74	0.800	0.817	0.875	0.055	0.075	0.034
0.1	0.07	72	0.799	0.816	0.874	0.055	0.076	0.034
0.1	0.1	72	0.798	0.815	0.873	0.056	0.077	0.035

Regarding parameters, Iter. = number of iterations, Step. = step size and Weig. = regularisation weight. W = segmented water, F = segmented fat and M = merged segmentations of water and fat.

Regarding evaluation of the deformation field, a heatmap for mean zeros in Jacobian ratio is shown in figure 4.14. All values regarding the Jacobian is shown in table 4.7.

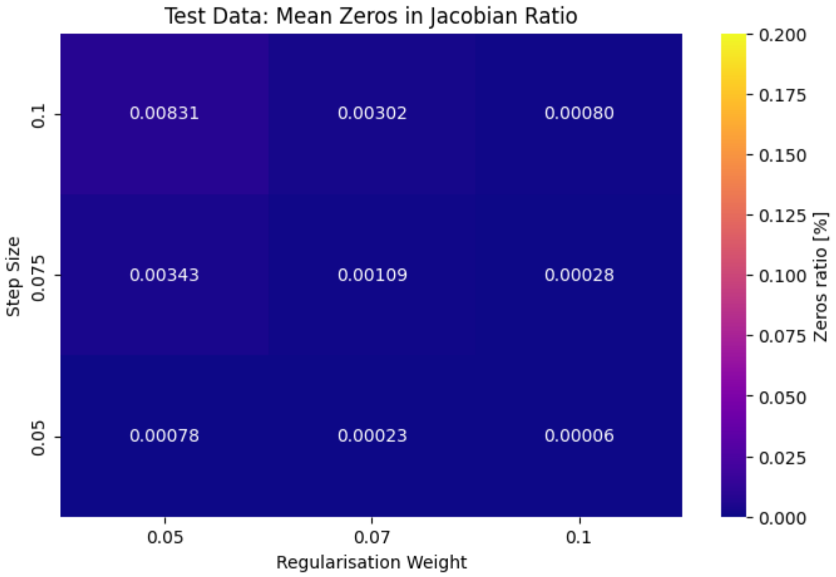

Figure 4.14: Heatmap of mean zeros in Jacobian ratio, with pyramid (1,6), 10 iterations and affine transformation in pre-registration.

A box plot of the zeros in Jacobian ratio of the test data is shown in figure 4.15. Some distinctive outliers can be identified.

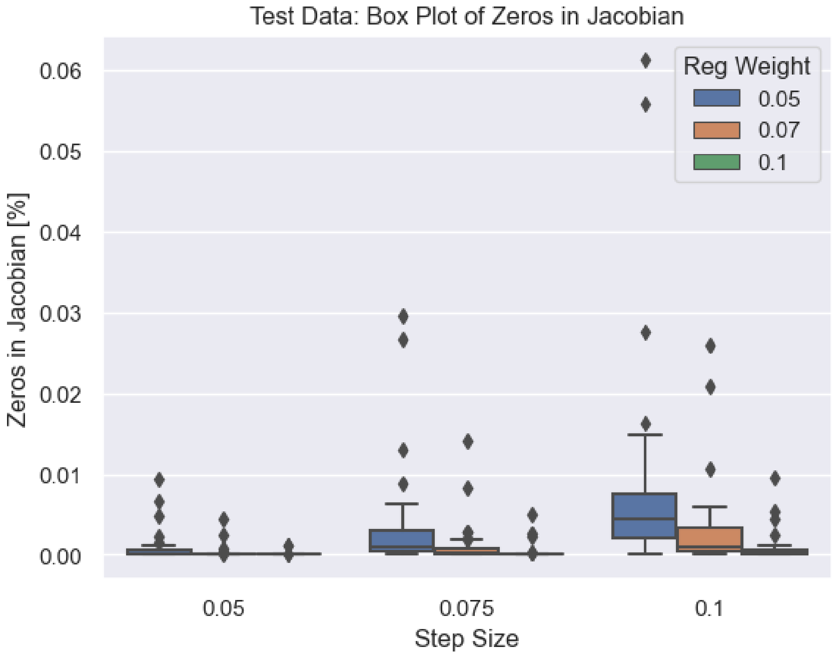

Figure 4.15: Box plot of the ratio of zeros in the Jacobian determinant, for the different parameter settings for test data.

Table 4.7: Scores for evaluating Jacobians. Pyramid levels (1,6) and 10 iterations.

Parameters		Jacobian	
Step.	Weigh.	Zeros in Jacobian ratio [%]	Jacobian mean
0.05	0.05	0.00078	0.14635
0.05	0.07	0.00023	0.14635
0.05	0.1	0.00006	0.14635
0.075	0.05	0.00343	0.14635
0.075	0.07	0.00109	0.14635
0.075	0.1	0.00028	0.14634
0.1	0.05	0.00831	0.14635
0.1	0.07	0.00302	0.14635
0.1	0.1	0.00080	0.14634

Iter. = number of iterations, Step. = step size and Weig. = regularisation weight.

4.1.3 Visual Evaluation

Firstly, two examples of sets with and without motion is presented. Figure 4.16 presents the magnitude of the displacement field of a set. The magnitude is low for all four time points, indicating no considerable difference between the time points and the reference image in the transformation. However, the area around the heart shows a higher magnitude for the majority of the time points.

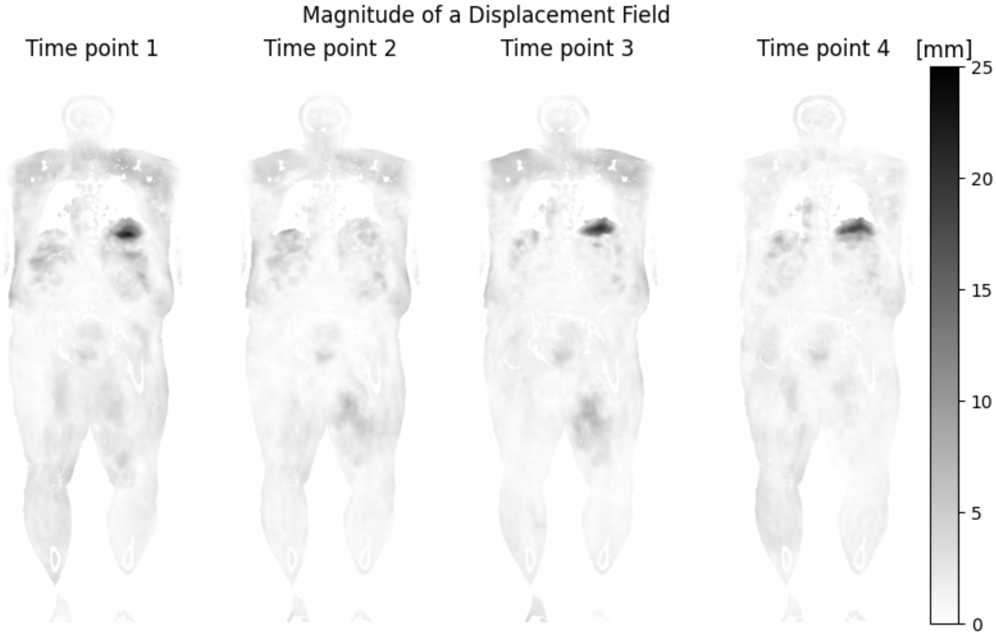

Figure 4.16: Magnitude of displacement field of a set without movement, with parameter settings pyramid (1,6), 10 iterations, step size 0.05, and regularisation weight 0.1.

Figure 4.17 presents another set, and shows a larger magnitude for the first three time points, indicating a motion between time point 3 and 4.

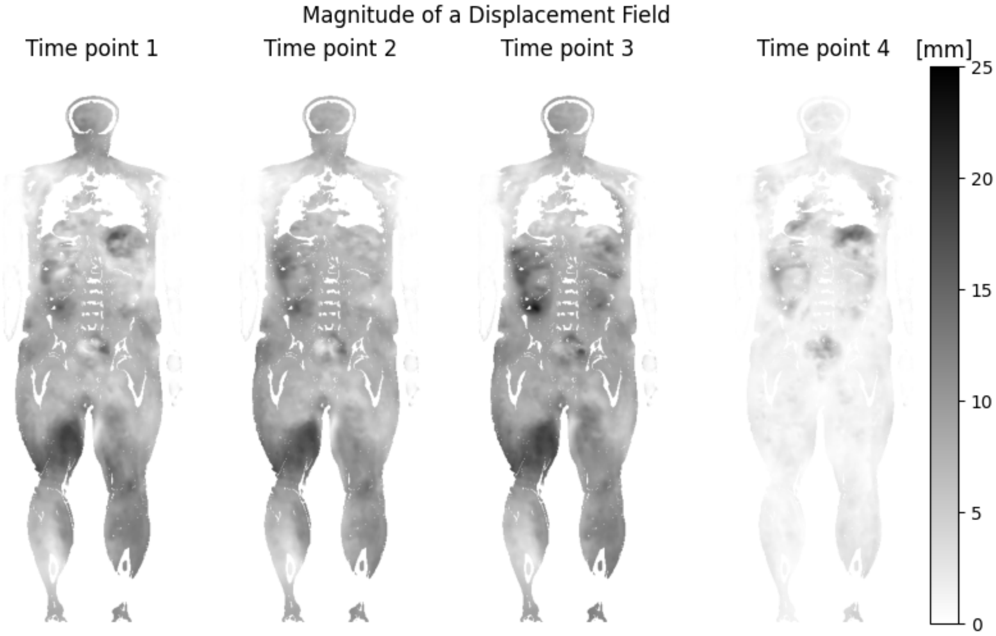

Figure 4.17: Magnitude of displacement field of a set with movement, with parameter settings pyramid (1,6), 10 iterations, step size 0.05, and regularisation weight 0.1.

In the box plot of zero ratio in Jacobian of the test data, in figure 4.15, some outliers could be identified. The most distinctive outliers were found to be time point 1 and 2 in one of the sets. When studying both the MR images and the magnitude of the displacement field of this set, it could be seen that there had been a large movement between time point 2 and 3. This is shown in figure 4.18, where the magnitude is large for the first and second time point, and small for the two later time points. Notice the change in value for the grey scale compared to the previous magnitude plots (a maximum of 90 mm compared to a previous maximum of 25 mm), indicating a greater motion with an increased maximum value.

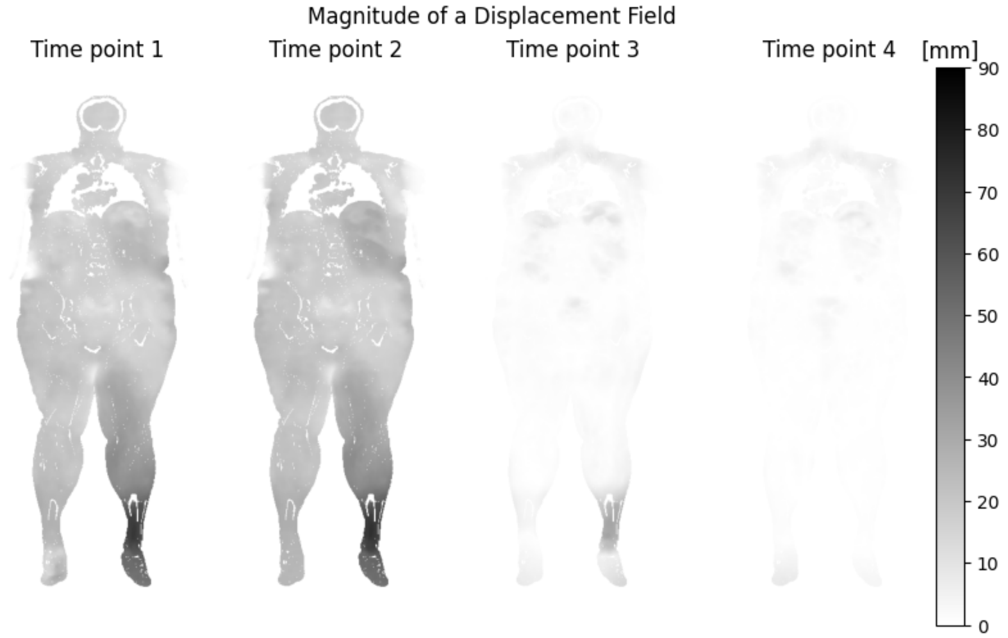

Figure 4.18: Magnitude of displacement field of a set with large movement, with parameter settings pyramid (1,6), 10 iterations, step size 0.05, and regularisation weight 0.1.

Multiple subjects with artifacts were observed in the MR data. In the box plot showing the zero ratio in Jacobian in phase 2, in figure 4.8, several outliers could be identified. The most distinctive outlier was found to be time point 4 in one of the sets. When studying these fat and water MR images, a swap in fat and water could be identified in the leg area above the knee. This was further investigated with a magnitude plot of the displacement field, shown in figure 4.19. The figure shows a large magnitude in this specific area, and the other time points are shown for reference.

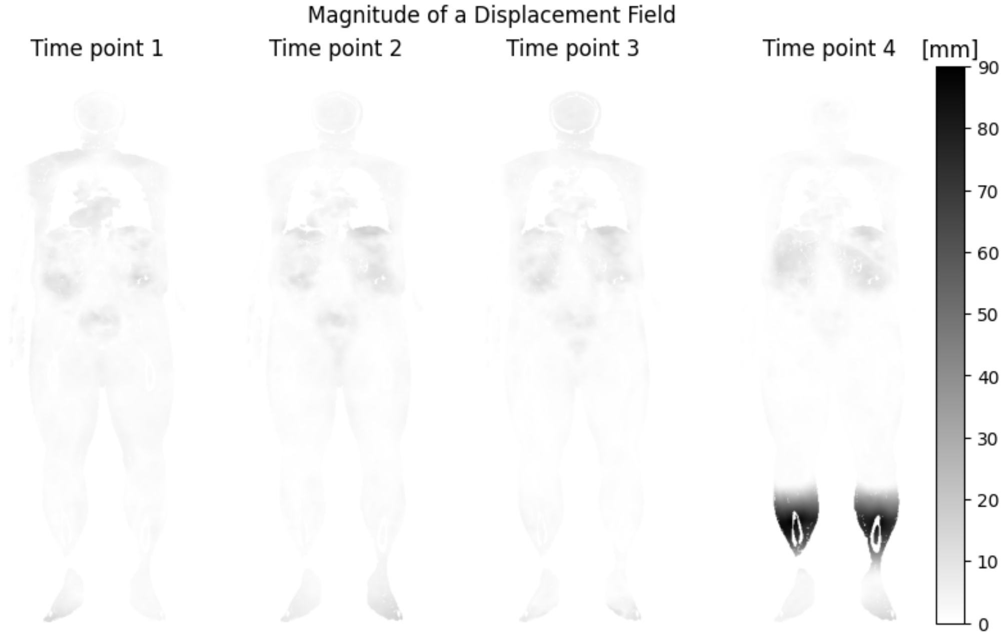

Figure 4.19: Magnitude of displacement field of a set with an artifact, with parameter settings pyramid (1,6), 10 iterations, step size 0.05, and regularisation weight 0.1.

4.2 Applying Motion Correction to PET Data

The following section presents the results regarding the PET modelling. First, the overall result for the Patlak modelling is presented, followed by more detailed results regarding unique subjects and segmentations.

4.2.1 General Patlak Results

The initial results for the PET modelling includes the overall mean for the relative standard error (RSE) of fitted K_i. The result for the different transforms is presented in figure 4.20, for all subjects and all tissue segmentations except pancreas. The pancreas was excluded from all results due to poor quality of these segmentations. The figure shows that the modelling for the transformed data is slightly varying, in degrees of error compared to the non transformed data. The transformed data also shows smaller error than the non transformed.

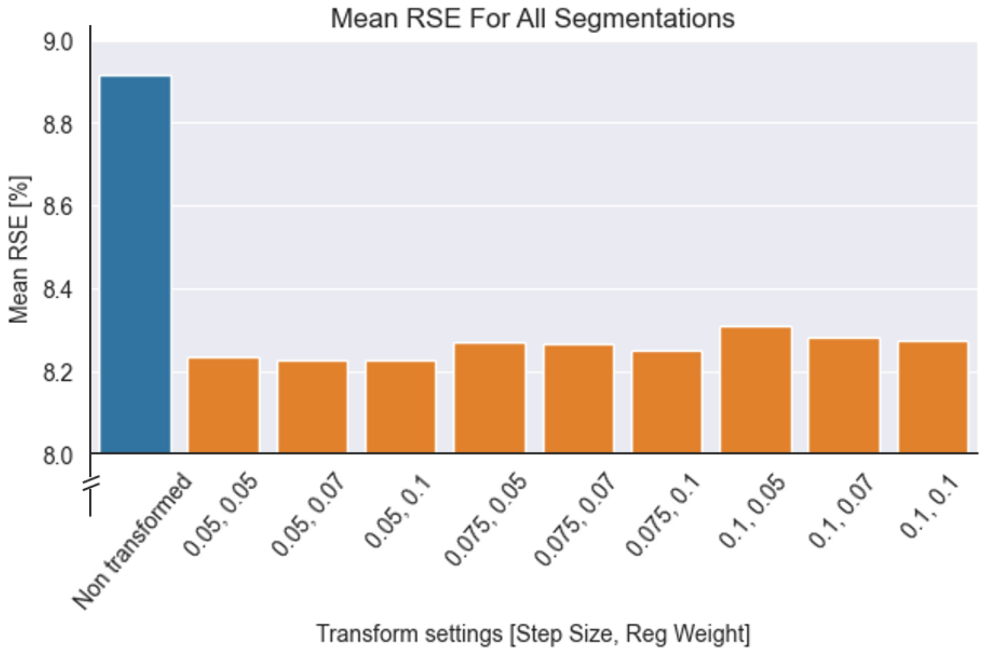

Figure 4.20: Mean results for Patlak RSE for all tissue segmentations except pancreas. Parameter settings pyramid (1,6) and 10 iterations, step size and regularisation weight as shown in figure.

4.2.2 Patlak for Individual Tissue Segmentations

The mean RSE values of the fitted K_i of the tissue segmentations were evaluated for the groups with and without motion. Figure 4.21 shows the result for the sets without motion, excluding the segmentation for pancreas. The bar plot shows that the RSE is similar with and without transformation for most of the segmentations. The exeptions are myocardium where the RSE increase with transformation, and vat where the RSE decrease with transformation. Overall, it can also be observed that vat shows the highest RSE value, and brain, lquad and rquad shows the lowest.

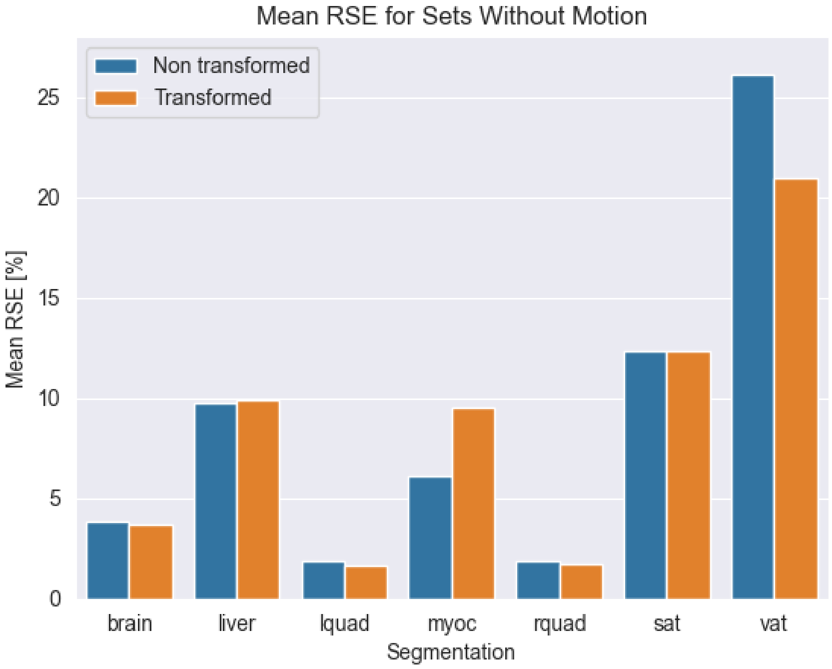

Figure 4.21: Mean Patlak RSE for different segmentations for all sets without motion. Parameter settings pyramid (1,6), 10 iterations, step size 0.05, and regularisation weight 0.1.

For the sets with motion, figure 4.22 shows the mean RSE for different segmentations. The figure shows that the mean RSE decrease with transformation compared to without transformation, for most of the segmentations. The largest decrease can be observed with the vat segmentation. The mean RSE value of the liver segmentation is the only one that increase with transformation.

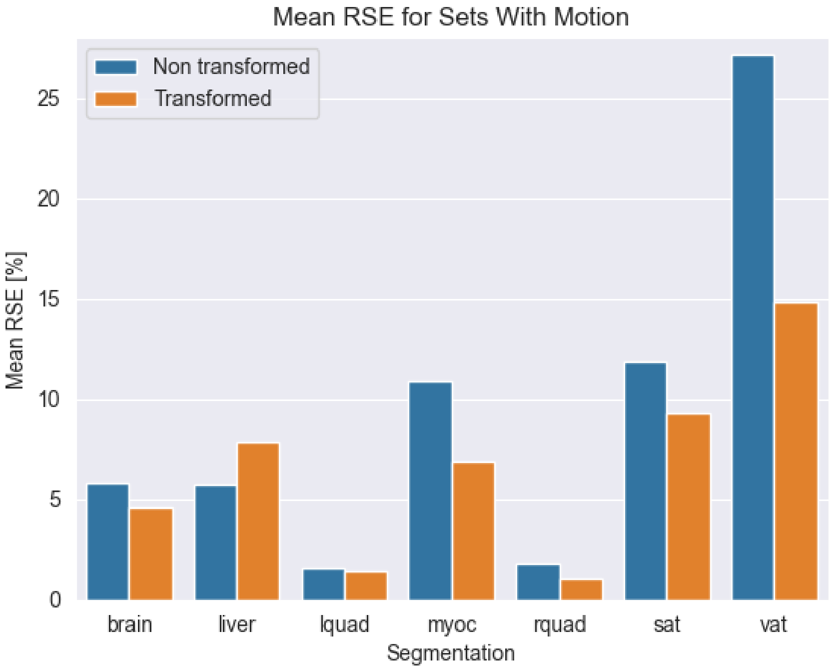

Figure 4.22: Mean Patlak RSE for different segmentations for all sets with motion. Parameter settings pyramid (1,6), 10 iterations, step size 0.05, and regularisation weight 0.1.

Similarly to the mean RSE values in the previous plots, the mean K_i values were also calculated and is presented in table 4.8. The dataset was divided into the same groups as before, and is presented separately as with and without motion. Both are compared to values for transformed and non transformed data. A difference in mean K_i value can be observed between the sets with and without motion. It is only a small difference between transformed and non transformed data within the groups.

Table 4.8: Mean K_i for sets with and without motion.

Segmentation	Mean K_i [ml/cm^3/min]			
	Without motion		With motion	
	Non trans.	Trans.	Non trans.	Trans.
brain	0.02082	0.02080	0.01720	0.01688
liver	0.004638	0.004650	0.004134	0.003972
lquad	0.007595	0.007587	0.008733	0.008692
rquad	0.007378	0.007367	0.008046	0.008036
myoc	0.05105	0.05135	0.05102	0.04882
sat	0.001638	0.001632	0.001668	0.001740
vat	0.001626	0.001746	0.001536	0.001734

Trans. = transformed.

4.2.3 Visual Evaluation

Figure 4.23 shows fused PET/MR images, of a representative slice of a 3D volume, with segmentations for brain, liver, rquad and lquad. The moving image corresponds to the first image in a set containing considerable motion and the reference is the fifth image of the same set. The transformed image is the result from applying a transformation on the moving image. Here the parameter setup of the transform was pyramid (1,6), 10 iterations, step size 0.05, and regularisation weight 0.1, with affine transform in pre-registration. Note that no signal was removed, but since the figure only shows one slice, a part of the signal could have been moved to another slice.

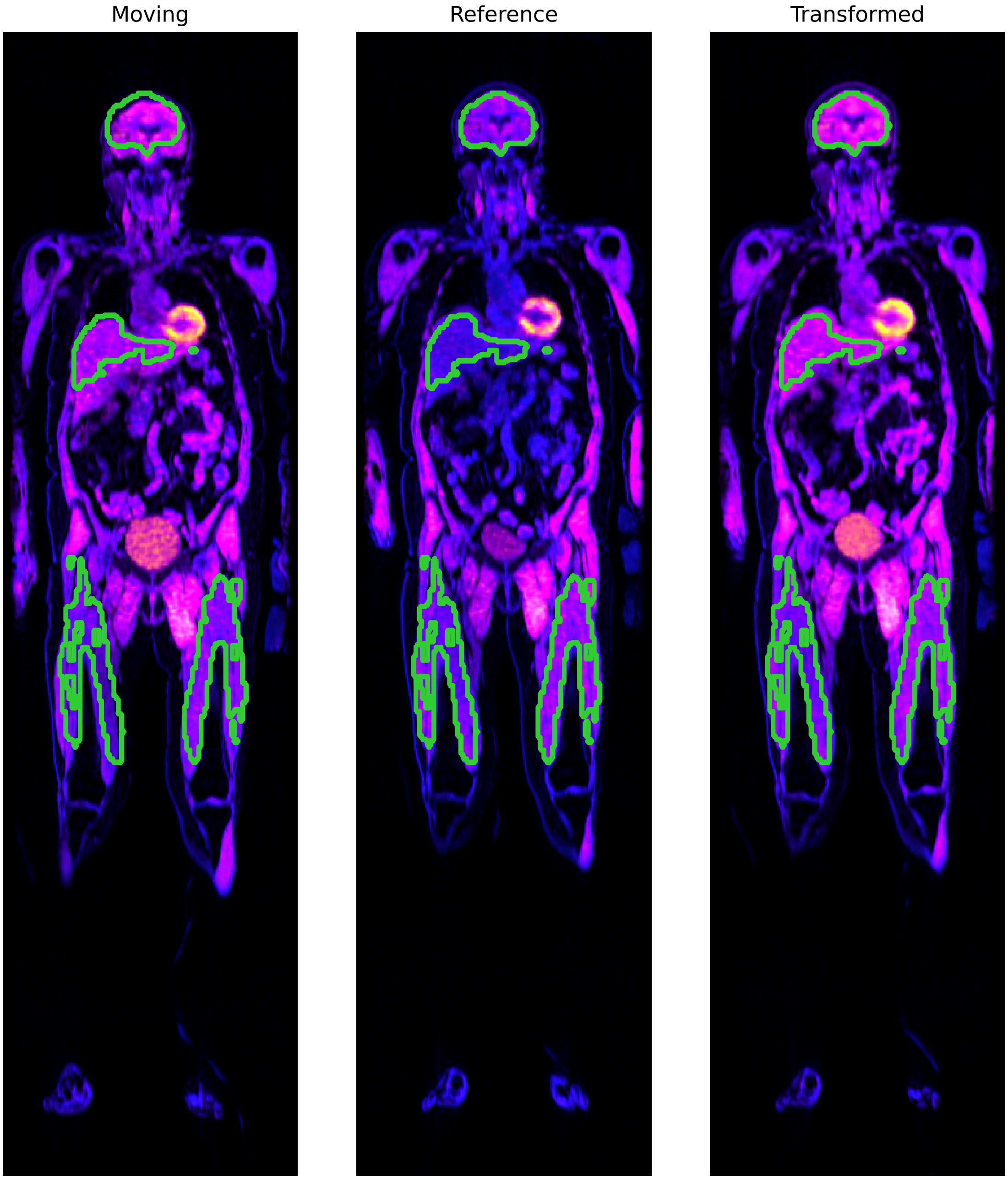

Figure 4.23: Fused PET/MR images, of a representative slice of a 3D volume, with marked segmentations for brain, liver, lquad and rquad, for the moving, reference and transformed image.

5

Discussion

In the following chapter, the results regarding both image registration on MR images and PET modelling are discussed, along with recommendations for future studies. As there is limited research regarding motion correction of bulk motions for dynamic whole-body PET/MR datasets post-reconstruction, the discussion focuses on aspects regarding the implemented method, rather than comparing alternative methods.

The dataset used in this study is unique and with its five anatomical reference images it gives opportunities for motion correction that for example PET/CT data with only one anatomical reference image does not have. It also implies that this method is not suitable for data with only one reference image. However, the motion correction method that has been introduced for a study using PET/CT could possibly be implemented for this type of dataset, where the motion is estimated from a dynamic PET data [41]. Further, the introduced method using rigid motion correction is implemented on PET/MR images and was shown to work well for head motions [5]. However, the assumption of a rigid body does not hold for this study of whole-body images with a considerable amount of soft tissue. Then there are multiple studies made for motion correction before or during reconstruction, but these are not applicable for this already reconstructed dataset [6][7].

5.1 Image Registration of MR Images

The method of using fast graph-cut based optimisation as image registration method shows promising results for this dataset of large volume medical MR images. There is an increase in terms of Dice score overall, which implies improved overlap of the images after the transformation is applied. However, evaluating the ratio of zeros in the Jacobian, there are some parameter setups that seems more promising than others. It should be noted that the optimisation of parameters is specific for this dataset and may vary to some extent for other datasets. Specifically regarding datasets with other types of motion, or varying degree of motion.

5.1.1 Optimisation

As results show, the Dice scores for water and fat segmentations follows the same trends between the different parameter setups. Therefore will the result be discussed more generally regarding the Dice scores. Starting with phase 1, it was seen that rigid and affine transformation in the pre-registration step worked equally in terms of both Dice score and run time, as seen in figure 4.1. The choice of then continuing using only affine was made since it could be more suitable for non-rigid structures, which is the case for whole-body images. Regarding pyramid level it was clear in figure 4.2 that using pyramid levels (1,6) gave a better result in terms of Dice than (2,6). There was however an increase in run time for (1,6), which could be seen as a drawback. Then, there might also be an increased risk of folds when using the lower levels of the pyramid. The lowest levels registers details in the image, where there is more noise generally and the search-space is larger, thereof grater risk of folds. In figure 4.2 it was also seen that ten iterations should be enough to reach convergence, which then was proceeded with to reduce run time. Regarding step size and regularisation weight, it could be seen in figure 4.3 and 4.4 that there was an overall improvement of Dice score for all setups. However, the biggest improvement was seen for lower step sizes and regularisation weights, so these were the ones to be investigated further in the following phases.

For phase 2 there where also a considerable improvement of Dice score for all tested parameter setups, as seen in figure 4.5 and 4.6. However, looking at the zero ratio in the Jacobians there is a significant difference between the different setups, which is seen in figure 4.7. A too low regularisation weight gives a relatively high ratio of zeros in the Jacobian. This implies foldings, which gets more considerate with increased step size for the low regularisation weights. A step size of 0.05 and a regularisation weight around 0.1 seemed the most promising for this phase with regards to the zero ratio in the Jacobian.

Phase 3 was done to investigate whether or not an increased number of iterations was needed for the smaller step sizes and regularisation weights. It was seen in figure 4.9, 4.10 and 4.11 that it was not, and seems to converge within ten iterations. Since the Dice scores were similar to those in phase 2 and that there were no improvement in zero ratio, there were no further investigation from phase 3.

5.1.2 Validation

A part of the dataset was used for validation, due to the used dataset being relatively small and the number of sets with considerable motion were few. After the dataset was randomly divided into training and testing it was checked that both included sets with known motion. This to not optimise for no subjects with considerable motion or to optimise for them all and not to have any to validate with. Validation of the method with the test data showed similar behaviour regarding both Dice scores and zero ratio in the Jacobian.

It should be noted when discussing considerable motion it is not specified which type, and sets with known motion varied mostly between head, legs and whole upper-body. Another implication of having a relatively small dataset is that it is not extensive enough for statistical evaluation. Hence the image registration part is limited to evaluating with overlap metrics and evaluation of the displacement fields, along with visual evaluation.

5.1.3 The Quality of Fat and Water Segmentations

The segmentations that were made to evaluate the registration could be a source of error. The automatic segmentations did include objects in the image space which was not a part of the imaged body. This included intravenous tubes and bags of water under the feet to increase signal, among other things. These were manually removed. Then, there were cases were the arms were not covered by the image space. Since this varied a lot between sets it was decided to remove them manually as well. This may have caused some errors, but are believed to be equivalent for all sets and should therefore not affect the overall result. Since the MR images were MRAC-based, their resolution is relatively low and could also be an source of error for the accuracy of the segmentations.

5.1.4 Evaluation Metrics and Effect of Artifacts

A drawback of using Dice score as an evaluation metric is that it is highly dependent on the size of the regions. An error for a single voxel can give a considerate error for small regions. Regarding the dataset used in this study, there is a variety in size between the subjects and thereby variety in size of the segmentations used for the evaluation with Dice. However, the segmentations are all of whole-body (arms excluded) and in the same order in terms of number of voxels in each segmentation. A limitation of using Dice on whole-body segmentations is that it is a relatively rough evaluation. It would be more preferable to do per organ, as like the ones used in the PET part, but this would be much more costly regarding computational time.

The goal with using the zero ratio in the Jacobian as an evaluation metric is to find those with ≤ 0 number of zeros, since zeros imply impossible physical transformations. However, there are some aspects in this study that makes it a bit more complex than only choosing the ones with no zeros. In the dataset there are multiple MR images where there has been fat-water swaps for some parts of the image. These parts are relatively small compared to the whole image, but within these parts it will try to register structures that does not correspond to the reference image. Consequently registering fat against water or vice versa. Then, the assumptions of the signal regarding the similarity metric does not hold in these regions. Note that this study uses the already reconstructed images, with no possibility of changing the signals correctly. So the aim was then to find a transformation that gives significant improvement in terms of Dice and a small ratio of zeros for all the sets in the dataset. It should be noted that the figures showing the ratio of zeros are mean values, for the whole training or test set. It could in many cases be seen that the zero ratio for an individual image was zero, but for some it was not. The images with artifacts such as fat-water swaps were often represented in those with zeros, which was seen in the box plot in figure 4.8. It should also be noted that it was not the objective of this study to further investigate additional registration parameters that gives best result in terms of the zero ratio in the Jacobian.

Regarding the magnitude plots shown in section 4.1.3 it can be seen that they vary considerably between the presented sets. This is likely because of the varying degree and type of motion between the sets, but also because of the artifacts from switched signals. As previously mentioned, no correspondence between the structures for the parts with swapped signal, which is not reasonable to register. This is clearly shown in the magnitude plot in figure 4.19. With the magnitude plots it is also clear between which time points the movement has occurred. As seen in figure 4.18, there has been considerable motion between time point two and three. It should also be noted that the magnitude plots generally looks reasonable regarding the whole dataset.

5.2 Applying Motion Correction to PET Data

The result of applying motion correction to the PET data showed promising differences on the sets with motion, and had less effect on those without. Evaluating the overall mean RSE for all segmentations showed a decrease in RSE for all parameter setups, presented in figure 4.20. Note that this is an overall decrease and does not show improvement for any organ specifically. It does however indicate an improvement of the localisation of the segments with motion correction.

The transform setting chosen for evaluating individual organs and visual evaluation of the motion correction on PET was based on the most promising results on phase 2. Since the Dice score was similar for the different transformations in phase 2, the chosen transformation was based on minimising the ratio of zeros in the Jacobian. The optimisation was made on the MR data since it is a better reference of the anatomy. However, the performance of the transform can differ when used on the PET data since that is a different problem. Therefore, the optimal parameter settings in regards to the PET data may need further investigation. Additionally, the optimal parameter settings can differ to other datasets.

5.2.1 Motion Correction on Segmented Tissues

The affect of motion correction was visually presented in figure 4.23. In the figure, the segmentations for brain, liver, and right respectively left quadriceps femoris muscle shows an improved alignment. This is shown when comparing the reference image to the moving and transformed image respectively. Therefore the motion correction seems to improve the location of these segmentations in sets with motion. For a small dataset like in this study, it would be possible to primarily use visual inspection in the evaluation. However, for studies with much larger number of subjects/scans, a visual inspection of all images would be considerably time consuming.

The result from the PET evaluation is dependent on the division of the dataset. The dataset was divided into groups with and without motion based on Dice score from the MR data. Multiple sets with low Dice score was found to be due to artifacts, or movement in areas outside of the PET segmentations. Manual inspection was therefore needed as well. There is no easy way to determine specific movements based on Dice score, other methods could therefore be more suitable. Furthermore, only five of the 32 sets were found to have considerable motion in the segmented areas, leading to difficulty using statistical methods in the evaluation. However, some trends could be identified.

Regarding the sets without motion, the mean RSE values were similar for the non transformed and transformed data, shown in figure 4.21. The result is desirable since there are no considerable movements, hence no motion correction is needed. The exceptions were the segmentations for myocardium and visceral adipose tissue, where the mean RSE value increased respectively decreased. The increased mean RSE value for myocardium may be explained by its strong signal and both cardiac and respiratory motion effects that were not possible to correct in this dataset. The decreased mean RSE value for visceral adipose tissue may be explained by the natural movement of intestines, and potential improvement for fat localisation to match the reference image created segmentation.

In regards of the sets with motion, the mean RSE value decreased for almost all segments, as shown in figure 4.22. The results indicates an improvement in the Patlak slope fit, hence possibly a potential of more accurate readouts from the PET data. Only exception was the liver, where an increase in the mean RSE was observed. This may be explained by the breathing motion and the risk of spillover signal from the myocardium. Another aspect when interpreting these results is the fact that it is the mean RSE value for the two groups, and it can therefore differ for the individual sets. A larger amount of sets in both groups, and especially the group with considerable motion, could lower the effect of these variations.

The results on uptake rate K_i, in table 4.8, show similar difference as the mean RSE differs in figure 4.21 and 4.22, for non transformed and transformed data with and without motion. The observation is reasonable since the segments unaffected of movement should keep the same net influx rate regardless if motion correction is applied or not. When comparing the calculated K_i values to the results from the original study, it also shows similar values [8].

5.2.2 Quality and Localisation of Tissue Segmentations

The quality and correct localisation of the tissue segmentations used have an effect on the PET kinetic readout. The evaluation (of motion correction) was performed on previously defined tissue segments, relevant for the clinical study. The eight segmentations were introduced in figure 3.2. However, the results from the pancreas segmentation were discarded from the results due to its poor anatomical reference on the MRAC images. One reason for the deficient anatomical localisation of the pancreas segmentation is that there is no true reference for this tissue in the MR images.

In order to fully evaluate the performance of the motion correction, more segments could have been added, which can be seen as future work. Some of the movements in the sets were identified in the feet, but since there were no available segmentations for that part of the anatomy, these sets were seen as without motion. Furthermore, regarding the sets with motion, the location of the movements varied. The range of possible bulk motion also decreased since the arms were removed from this dataset.

An alternative approach for evaluating K_i could involve a fully manual analysis, i.e. no motion correction but segment every time point separately. It may be a method for the most accurate readouts, but that would require considerably accurate work regarding the segmentations and would also be costly overall.

5.3 Future Work

In order to test this method further, it would be important to study a larger dataset, including sets with a wider range of bulk motions. This could give a better understanding of which parameter setups are efficient for bulk motions specifically. Also, using a more extensive dataset would give the opportunity of statistical evaluation.

More specifically regarding the image registration method there are some aspects that could be evaluated further. Using an additional evaluation metric such as inverse consistency could be an improvement. This in terms of ensuring that the transformations corresponds to a consistent and unique mapping between the two registered images. Future studies could also evaluate for which parameter setups gives the best result in terms of zero ratio in the Jacobians.

Regarding PET, creating more accurate tissue segmentations could improve the quantification of the motion correction. The segmentations could then be created in areas where there is better tissue contrast, such as the heart and liver. Further investigation of the optimal parameter settings for the transformation could improve the motion correction performance. Additional evaluation metrics could also be useful for this optimisation. The location of the available PET segmentations also limited the investigation of bulk motions in this study. Future work could therefore involve PET segmentations covering a wider range of bulk motions, which depends on what is clinically relevant for the specific study.

6

Conclusion

This study implemented an approach for bulk motion correction of a dynamic whole-body PET/MR dataset with promising results. The dataset allowed motion correction over time and estimation of the motion first on the MR and also to PET readouts. The MR registration was evaluated with Dice score and zero ratio in the Jacobian, which were used to find the more promising parameter setups. The motion correction applied to PET data was evaluated and sets with distinctive bulk motion showed improved alignment with its corresponding reference image, as well as decreased error in the Patlak slope fit. Furthermore, the motion correction seemed to not have a negative influence on the sets without major bulk motion overall.

Bibliography

[1] I. Polycarpou, G. Soultanidis, and C. Tsoumpas, "Synergistic motion compensation strategies for positron emission tomography when acquired simultaneously with magnetic resonance imaging," *Philosophical Transactions of the Royal Society A: Mathematical, Physical and Engineering Sciences*, vol. 379, 2204 Aug. 2021, ISSN: 1364-503X. DOI: `10.1098/rsta.2020.0207`.

[2] S. Ekström, F. Malmberg, H. Ahlström, J. Kullberg, and R. Strand, "Fast graph-cut based optimization for practical dense deformable registration of volume images," *Computerized Medical Imaging and Graphics*, vol. 84, p. 101 745, 2020, ISSN: 0895-6111. DOI: `https://doi.org/10.1016/j.compmedimag.2020.101745`.

[3] A. Rahmim, M. A. Lodge, N. A. Karakatsanis, *et al.*, "Dynamic whole-body PET imaging: principles, potentials and applications," *European Journal of Nuclear Medicine and Molecular Imaging*, vol. 46, pp. 501–518, 2 Feb. 2019, ISSN: 1619-7070. DOI: `10.1007/s00259-018-4153-6`.

[4] P. Summers, G. Saia, A. Colombo, *et al.*, "Whole-body magnetic resonance imaging: technique, guidelines and key applications," *ecancermedicalscience*, vol. 15, Jan. 2021, ISSN: 17546605. DOI: `10.3332/ecancer.2021.1164`.

[5] P. M. Johnson, R. Taylor, T. Whelan, J. D. Thiessen, U. Anazodo, and M. Drangova, "Rigid-body motion correction in hybrid PET/MRI using spherical navigator echoes," *Physics in Medicine & Biology*, vol. 64, 08NT03, 8 Apr. 2019, ISSN: 1361-6560. DOI: `10.1088/1361-6560/ab10b2`.

[6] C. Kolbitsch, C. Prieto, C. Tsoumpas, and T. Schaeffter, "A 3D MR-acquisition scheme for nonrigid bulk motion correction in simultaneous PET-MR," *Medical Physics*, vol. 41, no. 8Part1, p. 082 304, Jul. 2014, ISSN: 00942405. DOI: `10.1118/1.4890095`. [Online]. Available: `http://doi.wiley.com/10.1118/1.4890095`.

[7] M. G. Ullisch, J. Scheins, C. Weirich, *et al.*, "MR-guided data framing for PET motion correction in simultaneous MRPET: A preliminary evaluation," *Nuclear Instruments and Methods in Physics Research Section A: Accelerators, Spectrometers, Detectors and Associated Equipment*, vol. 702, pp. 67–69, 2013, ISSN: 0168-9002. DOI: `https://doi.org/10.1016/j.nima.2012.09.033`. [Online]. Available: `https://www.sciencedirect.com/science/article/pii/S016890021201090X`.

[8] E. Johansson, M. Lubberink, K. Heurling, *et al.*, "Whole-Body Imaging of Tissue-specific Insulin Sensitivity and Body Composition by Using an Inte-

grated PET/MR System: A Feasibility Study," *Radiology*, vol. 286, pp. 271–278, 1 Jan. 2018, ISSN: 0033-8419. DOI: `10.1148/radiol.2017162949`.

[9] C. S. Patlak, R. G. Blasberg, and J. D. Fenstermacher, "Graphical Evaluation of Blood-to-Brain Transfer Constants from Multiple-Time Uptake Data," *Journal of Cerebral Blood Flow & Metabolism*, vol. 3, pp. 1–7, 1 Mar. 1983, ISSN: 0271-678X. DOI: `10.1038/jcbfm.1983.1`.

[10] M. Chappell, *Principles of Medical Imaging for Engineers*. Springer International Publishing, 2019, ISBN: 978-3-030-30510-9. DOI: `10.1007/978-3-030-30511-6`. [Online]. Available: `http://link.springer.com/10.1007/978-3-030-30511-6`.

[11] J. L. Prince and J. M. Links, *Medical Imaging Signals and Systems*, 2nd ed. Pearson, 2015, ISBN: 978-0-13-214518-3.

[12] J. Ma, "Dixon techniques for water and fat imaging," *Journal of Magnetic Resonance Imaging*, vol. 28, pp. 543–558, 3 Sep. 2008, ISSN: 10531807. DOI: `10.1002/jmri.21492`.

[13] H. H. Hu, P. Börnert, D. Hernando, *et al.*, "ISMRM workshop on fat-water separation: Insights, applications and progress in MRI," *Magnetic Resonance in Medicine*, vol. 68, pp. 378–388, 2 Aug. 2012, ISSN: 07403194. DOI: `10.1002/mrm.24369`.

[14] Oikonen, Vesa, *PET image*, Turku PET centre. [Internet]. 2018. [Cited 29th April 2023]. Available from: `http://www.turkupetcentre.net/petanalysis/image_pet.html`.

[15] R. Zimmermann, *Nuclear Medicine : Radioactivity for Diagnosis and Therapy*, 2nd ed. EDP Sciences, 2020, pp. 101–104, ISBN: 978-2-759-82149-5. [Online]. Available: `https://ebookcentral.proquest.com/lib/chalmers/detail.action?docID=5024612`.

[16] R. Boellaard, M. J. ODoherty, W. A. Weber, *et al.*, "FDG PET and PET/CT: EANM procedure guidelines for tumour PET imaging: version 1.0," *European Journal of Nuclear Medicine and Molecular Imaging*, vol. 37, pp. 181–200, 1 Jan. 2010, ISSN: 1619-7070. DOI: `10.1007/s00259-009-1297-4`.

[17] G. Fahrni, N. A. Karakatsanis, G. D. Domenicantonio, V. Garibotto, and H. Zaidi, "Does whole-body Patlak 18F-FDG PET imaging improve lesion detectability in clinical oncology?" *European Radiology*, vol. 29, pp. 4812–4821, 9 Sep. 2019, ISSN: 0938-7994. DOI: `10.1007/s00330-018-5966-1`.

[18] Jødal, Lars, *Interpretation of the Patlak plot*, Turku PET centre. [Internet]. 2014. [Cited 26th April 2023]. Available from: `http://turkupetcentre.net/petanalysis/model_patlak_interpretation.html`.

[19] Y. Zuo, J. Qi, and G. Wang, "Relative Patlak plot for dynamic PET parametric imaging without the need for early-time input function," *Physics in Medicine & Biology*, vol. 63, p. 165 004, 16 Aug. 2018, ISSN: 1361-6560. DOI: `10.1088/1361-6560/aad444`.

[20] B. Bogdanovic, E. L. Solari, A. V. Asiares, *et al.*, "PET/MR Technology: Advancement and Challenges," *Seminars in Nuclear Medicine*, vol. 52, pp. 340–355, 3 May 2022, ISSN: 00012998. DOI: `10.1053/j.semnuclmed.2021.11.014`.

[21] J. A. Disselhorst, I. Bezrukov, A. Kolb, C. Parl, and B. J. Pichler, "Principles of PET/MR Imaging," *Journal of Nuclear Medicine*, vol. 55, 2S–10S, Supplement 2 Jun. 2014, ISSN: 0161-5505. DOI: `10.2967/jnumed.113.129098`.

[22] J. Liu and J. Geng, "Recent progress on imaging technology and performance testing of PET/MR," *Radiation Detection Technology and Methods*, Jan. 2023, ISSN: 2509-9930. DOI: `10.1007/s41605-022-00376-8`.

[23] Y. Petibon, C. Ma, J. Ouyang, and G. El Fakhri, "Cardiac pet/mr basics," in *FDG-PET/CT and PET/MR in Cardiovascular Diseases*, M. Pelletier-Galarneau and P. Martineau, Eds. Cham: Springer International Publishing, 2022, pp. 21–35, ISBN: 978-3-031-09807-9. DOI: `10.1007/978-3-031-09807-9_2`. [Online]. Available: `https://doi.org/10.1007/978-3-031-09807-9_2`.

[24] C. Catana, "Chapter 34 - MR-assisted PET motion correction in PET/MR," in *Motion Correction in MR*, ser. Advances in Magnetic Resonance Technology and Applications, A. J. van der Kouwe and J. B. Andre, Eds., vol. 6, Academic Press, 2022, pp. 553–568. DOI: `https://doi.org/10.1016/B978-0-12-824460-9.00016-9`. [Online]. Available: `https://www.sciencedirect.com/science/article/pii/B9780128244609000169`.

[25] J. Ashburner and K. J. Friston, "Rigid body registration," *Statistical parametric mapping: The analysis of functional brain images*, pp. 49–62, 2007.

[26] A. Sotiras, C. Davatzikos, and N. Paragios, "Deformable medical image registration: A survey," *IEEE transactions on medical imaging*, vol. 32, no. 7, pp. 1153–1190, 2013.

[27] F. P. Oliveira and J. M. R. Tavares, "Medical image registration: A review," *Computer methods in biomechanics and biomedical engineering*, vol. 17, no. 2, pp. 73–93, 2014.

[28] P. Devadas, G. Kalaiarasi, and M. Selvi, "Intensity based Image Registration on Brain MRI Images," in *2020 Second International Conference on Inventive Research in Computing Applications (ICIRCA)*, IEEE, 2020, pp. 257–262.

[29] B. Glocker, A. Sotiras, N. Komodakis, and N. Paragios, "Deformable medical image registration: Setting the state of the art with discrete methods," *Annual review of biomedical engineering*, vol. 13, pp. 219–244, 2011.

[30] D. Rueckert, P. Aljabar, R. A. Heckemann, J. V. Hajnal, and A. Hammers, "Diffeomorphic registration using b-splines," in *Medical Image Computing and Computer-Assisted Intervention – MICCAI 2006*, R. Larsen, M. Nielsen, and J. Sporring, Eds., Berlin, Heidelberg: Springer Berlin Heidelberg, 2006, pp. 702–709, ISBN: 978-3-540-44728-3.

[31] F. Maes, D. Vandermeulen, and P. Suetens, "Medical image registration using mutual information," *Proceedings of the IEEE*, vol. 91, no. 10, pp. 1699–1722, 2003.

[32] A. A. Taha and A. Hanbury, "Metrics for evaluating 3D medical image segmentation: analysis, selection, and tool," *BMC Medical Imaging*, vol. 15, p. 29, 1 Dec. 2015, ISSN: 1471-2342. DOI: `10.1186/s12880-015-0068-x`.

[33] P. Bourke, "Cross correlation," *Cross Correlation, Auto Correlation2D Pattern Identification*, 1996.

[34] J. Martin and J. L. Crowley, "Experimental comparison of correlation techniques," in *Int. Conf. on Intelligent Autonomous Systems*, Citeseer, 1995.

[35] S. Klein, M. Staring, and J. P. Pluim, "Evaluation of optimization methods for nonrigid medical image registration using mutual information and B-splines," *IEEE transactions on image processing*, vol. 16, no. 12, pp. 2879–2890, 2007.

[36] Y. Boykov, O. Veksler, and R. Zabih, "Fast approximate energy minimization via graph cuts," *IEEE Transactions on pattern analysis and machine intelligence*, vol. 23, no. 11, pp. 1222–1239, 2001.

[37] S. Ekström, M. Pilia, J. Kullberg, H. Ahlström, R. Strand, and F. Malmberg, "Faster dense deformable image registration by utilizing both CPU and GPU," *Journal of Medical Imaging*, vol. 8, 01 Feb. 2021, ISSN: 2329-4302. DOI: `10.1117/1.JMI.8.1.014002`.

[38] A. A. Goshtasby, *Theory and applications of image registration*. John Wiley & Sons, 2017, pp. 343–352.

[39] L. R. Dice, "Measures of the Amount of Ecologic Association Between Species," *Ecology*, vol. 26, pp. 297–302, 3 Jul. 1945, ISSN: 00129658. DOI: `10.2307/1932409`.

[40] Y. Zhang, S. Liu, C. Li, and J. Wang, "Rethinking the dice loss for deep learning lesion segmentation in medical images," *Journal of Shanghai Jiaotong University (Science)*, vol. 26, pp. 93–102, 1 Feb. 2021, ISSN: 1007-1172. DOI: `10.1007/s12204-021-2264-x`.

[41] T. Sun, Y. Wu, W. Wei, *et al.*, "Motion correction and its impact on quantification in dynamic total-body 18F-fluorodeoxyglucose PET," *EJNMMI Physics*, vol. 9, p. 62, 1 Sep. 2022, ISSN: 2197-7364. DOI: `10.1186/s40658-022-00493-9`.

[42] B. C. Lowekamp, D. T. Chen, L. Ibáñez, and D. Blezek, "The design of simpleitk," *Frontiers in neuroinformatics*, vol. 7, p. 45, 2013.

[43] Ekström, Simon, *pydeform*, [Internet]. 2019. [Cited 23th Mars 2023]. Available from: `https://pypi.org/project/pydeform/`.

[44] K.-S. Chuang, H.-L. Tzeng, S. Chen, J. Wu, and T.-J. Chen, "Fuzzy c-means clustering with spatial information for image segmentation," *computerized medical imaging and graphics*, vol. 30, no. 1, pp. 9–15, 2006.

[45] F. Malmberg, R. Nordenskjöld, R. Strand, and J. Kullberg, "SmartPaint: a tool for interactive segmentation of medical volume images," *Computer Methods in Biomechanics and Biomedical Engineering: Imaging & Visualization*, vol. 5, no. 1, pp. 36–44, Jan. 2017, ISSN: 2168-1163. DOI: `10.1080/21681163.2014.960535`. [Online]. Available: `https://www.tandfonline.com/doi/full/10.1080/21681163.2014.960535`.

A

Appendix

A.1 Selection of Sets with Motion in MR Dataset

For the evaluation of applying motion correction to the PET data, selection of sets with motion was based on Dice score of the MR data. Table A.1 presents the sets, with fat and/or water Dice score lower than 0.56, and the observations found relating to the low spatial overlap score. Only the time point with the lowest Dice score for the respective set is presented.

Table A.1: Sets with low Dice score in MR dataset. Presenting original Dice score for water and fat, and type of movement or artifact and its location.

Dice Score		Observation	
Water	Fat	Type	Location
0.187	0.199	Movement	Whole body
0.480	0.200	Movement	Legs, head
0.625	0.313	Movement	Feet
0.609	0.355	Artifact	Lower leg, feet
0.385	0.475	Movement	Legs, feet, head
0.683	0.478	Movement	Upper body, part of legs
0.480	0.639	Movement	Feet
0.503	0.577	Artifact	Knee
0.508	0.638	Artifact	Lower leg
0.545	0.733	Movement	Lower legs
0.548	0.554	Movement	Legs
0.550	0.577	Artifact	Knees

DEPARTMENT OF ELECTRICAL ENGINEERING
CHALMERS UNIVERSITY OF TECHNOLOGY
Gothenburg, Sweden 2023
www.chalmers.se

CHALMERS
UNIVERSITY OF TECHNOLOGY